ASYMPTOTIC THEORY OF TWO-DIMENSIONAL TRAILING-EDGE FLOWS*

By R. E. Melnik and R. Chow
Grumman Aerospace Corportation

SUMMARY

In this investigation, problems of laminar and turbulent viscous interaction near trailing edges of streamlined bodies are considered. The laminar study is based on the triple-deck formulation of Stewartson, Messiter, and Brown. This theory is developed from asymptotic expansions of the Navier-Stokes equations in the limit of large Reynolds numbers. The expansions describe the local solution near the trailing edge of cusped or nearly cusped airfoils at small angles of attack in compressible flow. A complicated inverse iterative procedure, involving finite-difference solutions of the triple-deck equations coupled with asymptotic solutions of the boundary values, is used to accurately solve the viscous interaction problem. Results are given for the correction to the boundary-layer solution for drag of a finite flat plate at zero angle of attack. A solution is also presented for the viscous correction to the lift of an airfoil at incidence. A comparison of the present results with triple-deck solutions recently obtained by other investigators for the symmetric problem is presented. Also presented are some comparisons of the present solution with low Reynolds number ($R \leqq 200$) solutions of the Navier-Stokes equations and with experimental data. These comparisons indicate that the asymptotic triple-deck theories are accurate over a surprisingly wide range of Reynolds numbers down to Reynolds numbers as low as 10 or less.

In the second part of this investigation, the problem of turbulent interactions at airfoil trailing edges is considered. It is demonstrated that second-order boundary-layer theory fails at airfoil trailing edges and that the concept of the flow over an equivalent body formed from the displacement thickness is not appropriate for turbulent flows near trailing edges. A rational asymptotic theory is developed for treating turbulent interactions near trailing edges and is shown to lead to a multilayer structure of turbulent boundary layers. The flow over most of the boundary layer is described by a Lighthill model of inviscid rotational flow. The main features of the model are discussed and a sample solution for the skin friction is obtained and compared with the data of Schubauer and Klebanoff for a turbulent flow in a moderately large adverse pressure gradient.

*This research was performed under NASA Langley Contract No. NAS 1-12426.

INTRODUCTION

The problem of trailing-edge flows is of considerable importance in aerodynamics. Most streamlined bodies end in a sharp trailing edge that is cusped or nearly cusped in order to provide a smooth transition of the flow into the wake. The flow near the trailing edge is important in establishing the lift and drag forces on the body.

At high Reynolds numbers the solution of the Navier-Stokes equations can be expanded in descending powers (and logarithms) of the Reynolds number. The leading term is governed by inviscid flow equations over most of the domain and by boundary-layer equations in a thin layer near the surface and in the wake. To lowest order, the lift is determined by solutions of the inviscid-flow equations, subject to the Kutta condition. Skin-friction drag is determined by solutions of the boundary-layer equations with the pressure distribution obtained from the inviscid solution. Within this approximation, form drag is computed from the surface pressures induced by the effect of the boundary layer on the external inviscid flow and is, therefore, a second-order effect in the theory.

Although the inviscid and boundary-layer solutions provide the leading approximation for the flow over streamlined bodies, higher order corrections are important in many problems. A major impediment in the determination of the correction is due to the fact that the underlying asymptotic expansions are not uniformly valid at trailing edges. The nonuniformity is caused by the appearance of singularities in solutions of both the laminar and turbulent boundary-layer equations at trailing edges. The nature of the singularity differs in the laminar and turbulent cases, but in both cases, the major effect is the production of a displacement thickness that is singular at the trailing edge. This in turn leads to singularities in the induced pressures at the trailing edge. As a result, the second-order Kutta condition cannot be satisfied and the viscous correction to lift cannot be determined. In addition, corrections to the boundary-layer solutions for skin friction and form drag are not correctly determined by standard second-order boundary-layer theory. Most existing engineering methods for predicting viscous effects on lift are based on iterative solutions of the second-order boundary-layer equations. These methods experience difficulties at trailing edges which are circumvented by an ad hoc smoothing of the displacement surface determined from the solution of the boundary-layer equations.

In spite of its importance and the continuing interest of many investigators, it is only recently that a comparatively complete theory of trailing-edge flows has been developed and this only for laminar flows. The recent advances in laminar trailing-edge problems are based on the triple-deck formulation of Stewartson (ref. 1) and Messiter (ref. 2) developed originally for a symmetric flat plate at zero angle of attack. These theories were then extended the following year by Brown and Stewartson (ref. 3) to the lifting flat plate. The triple-deck theories are applicable to general airfoils with a cusped or nearly cusped

trailing edge in compressible flow. For Mach numbers not near one, compressibility enters into the theory only through a scaling of dependent and independent variables. However, even though a number of properties of the solution were determined and the singular behavior was explained, accurate numerical solutions were not obtained in these early works.

The first part of this paper deals with the laminar-viscous interaction near airfoil trailing edges in the limit of large Reynolds numbers. The approach used is to develop the appropriate numerical procedures to solve the boundary-value problem formulated by Stewartson, Messiter, and Brown. A general discussion of the laminar-flow problem along with a summary of the triple-deck formulation and the resulting boundary-value problem is presented in the section "The Laminar-Flow Problem." The following section, entitled "The Numerical Method," deals with all aspects of the numerical methods used to solve this problem. First, an inverse iterative scheme to solve the coupling between the various layers of the triple deck is discussed. Then finite-difference methods based on the Keller "box" scheme (refs. 4 and 5) are formulated to solve the triple-deck equations. Methods are also discussed for the evaluation of the Hilbert integrals arising from the analysis. Also presented in the section on numerical methods is a description of the accuracy and convergence properties of the numerical methods. A discussion of the results for both zero and nonzero incidence follows in the Results. Solutions to the symmetric problem have also been recently obtained by Jobe and Burggraf (ref. 6) and by Veldman and Van De Vooren (ref. 7). Detailed comparisons between the present solution and those of references 6 and 7 are provided. Also the solution for the drag of a finite flat plate at zero incidence is compared with the experimental data of Janour (ref. 8) and with finite-difference solutions of the complete Navier-Stokes equations recently obtained by S. C. R. Dennis, who provided numerical data from his unpublished results. The solution for the velocity profile in the wake of the symmetric solution is compared with experimental data of Sato and Kuriki (ref. 9).

Currently, understanding of turbulent interactions at trailing edges is rather less complete. Recent attempts to develop a rational theory of turbulent trailing-edge flows include the investigations of Spence (ref. 10) and Küchman (ref. 11). In reference 10, the main correction to boundary-layer theory is assumed to arise from the pressure change across the wake generated by the singular curvature of the inviscid trailing streamline. This leads to a jet-flap model of trailing-edge flows. Spence's model is inconsistent and leads to unacceptable oscillatory solutions downstream. The failure of Spence's theory is caused by the neglect of convective acceleration terms in the normal momentum equations. It is interesting that a scaling analysis of Spence's interaction equation indicates the need to retain these terms in the lowest order theory. The investigation of Küchman in reference 11 is based on a Lighthill model of turbulent boundary layers near the trailing edge, which is treated as an inviscid rotational flow. Some examples of rotational flow in

a wedge-shaped compression corner are presented. Although these results are of interest, there is no attempt to develop a complete, rational theory and no consideration is given to the trailing-edge region on a lifting airfoil.

A more promising approach for a rational theory of turbulent flows follows from asymptotic expansions of the time-averaged Navier-Stokes equations in the limit of large Reynolds numbers. Similar asymptotic techniques have been applied to noninteracting turbulent boundary layers by Mellor (ref. 12), Yajnik (ref. 13), and Bush and Fendell (refs. 14 and 15) and to transonic shock-wave—boundary-layer interactions by Melnik and Grossman (ref. 16) and by Adamson and Feo (ref. 17).

In the second part of the present investigation (Turbulent Trailing-Edge Flows) it is shown that asymptotic analysis leads to a three-layer description of turbulent interaction near trailing edges with a streamwise length scale that is on the order of a boundary-layer thickness. The flow in the outermost layer is governed by inviscid, linearized rotational-flow equations. The description near the wall requires two layers, involving just Reynolds stresses in the middle layer and both Reynolds and laminar stresses in the innermost wall layer. The solution in the outer layer is unaffected to lowest order by the two inner layers and can, therefore, be completely determined independently of the details of the inner layers. This leads to a Lighthill model for the outer problem that must be solved to determine the pressure distribution and lift forces. Here, only the incompressible problem will be considered and a brief description of the essential features of the interaction model, together with a formulation of a boundary-value problem governing the outer inviscid flow will be provided. Also a sample solution for the skin friction determined from matching the inner and outer solutions is given and the results are compared with the low-speed data of Schubauer and Klebanoff (ref. 18).

SYMBOLS

a_1, a_2 parameters related to lift coefficient and constant defined by equation (19b)

A displacement function in triple-deck theory

A_1^-, A_1^+ constants related to behavior of A near the origin

b_1 constant in asymptotic solution for $|X| \to \infty$

B_P constant defining y-grid distribution

B_α constant related to second-order boundary-layer solution for displacement thickness (turbulent)

C_f	skin-friction coefficient, $\dfrac{\tau_w^*}{\frac{1}{2}\rho U_\infty^2}$
$C_{f,o}$	skin-friction coefficient of noninteracting boundary-layer solution at trailing edge (turbulent)
C_{ij}	constant appearing in asymptotic solutions of triple-deck equations, where i and j = 1, 2, 3, . . .
C_L	lift coefficient
C_o	coefficient of singular pressure gradient in wake
C_α	constant related to singularity of inviscid solution near trailing edge
d	normalized shear stress gradient in computation plane, $\partial\tau/\partial y$
d_1	constant in asymptotic solution for $\lvert X\rvert \to \infty$
d_2	constant in triple-deck solution for drag coefficient
D	shear stress gradient in Z-direction, $\partial\tau/\partial Z$
f	Blasius function
F_1	similarity function related to symmetric triple-deck solution for $\lvert X\rvert \to -\infty$
G_o	Hakkinen-Rott similarity function related to triple-deck solution for $X \to 0$
h_1,h_2,h_3	functions appearing in differential equations for H_1, H_2, and H_3, respectively
H	shape factor, δ_1^*/δ_2^*
H_1,H_2,H_3	similarity functions related to triple-deck solutions for $X \to -\infty$
I	integer, running index for X-mesh
I_p	integer related to X-mesh

I_1, I_2, I_3 integers defining X-mesh

J integer, running index for y-mesh

J_{inner} number of points in inner mesh in wake

J_P number of mesh points in y-mesh on plate

J_W number of mesh points in y-mesh in wake

K_i parameter defining mesh distribution, where $i = 1, 2, \ldots$

$\ell(y^+)$ mixing length, turbulent flow

L length of plate or chord, dimensional

L_0, L_1, L_{max} parameters related to X-mesh

p pressure

p_∞ free-stream pressure, dimensional

P normalized pressure appearing in triple-deck theory

P_1, P_2, P_3 constants related to behavior of P near origin

R Reynolds number, $U_\infty L/\nu$

R_{ij} functions related to asymptotic behavior of U as $Z \to \infty$, where i and $j = 1, 2$

T_i integrals defined by equations (45), where $i = 1, 2, 3$

u velocity in streamwise direction

u_τ friction velocity, $\sqrt{\tau_w/\rho}$

U normalized velocity in streamwise direction in triple-deck theory

U_∞ free-stream velocity, dimensional

v	velocity in direction normal to plate
V	normalized velocity in direction normal to plate in triple-deck theory
W	Coles wake function (turbulent flow)
x	Cartesian coordinate along plate
X	normalized coordinate along plate in triple-deck theory
X_p	end point of boundary-layer calculation
y	computational coordinate normal to plate for laminar flow and physical coordinate for turbulent flow
y_M	coordinate defining outer boundaries of y-mesh
Z	physical coordinate normal to plate for laminar flow
α	normalized angle of attack in triple-deck theory
α^*	angle of attack in radians
γ	constant appearing in behavior of triple-deck solution near origin for $\alpha \neq 0$
$\Gamma(\ )$	Gamma function
δ	boundary-layer thickness
δ_1	displacement thickness
δ_2	momentum thickness
δ_c	boundary-layer camber, $\frac{1}{2}(\delta_T - \delta_B)$
ϵ	small parameter, $R^{-1/8}$ for laminar flow and $\sqrt{\frac{C_{f,o}}{2}}$ for turbulent flow
$\hat{\epsilon}$	small parameter related to wall-layer thickness, $(\epsilon^2 R)^{-1}$ in turbulent flow

ζ vorticity (turbulent flow); also variable defined by equations (38) and (39)

η independent variable in similarity solutions of triple-deck equations, $|Z|/2|2X|^{1/3}$

θ parameter used to scale wake location, related to wake centerline

κ Karman constant, approximately equal to 0.41

λ constant, equal to 0.33206, appearing in Blasius solution, f''(0)

λ_1 normalized skin friction at trailing edge in triple-deck solution

$\Lambda_{10}, \Lambda_{02}, \Lambda_{23}$ integrals defined by equations (46)

ν coefficient of kinematic viscosity, dimensional

ξ variable used in definition of X-grid distribution

$\tilde{\pi}$ Coles wake parameter

ρ density, dimensional

σ parameter used to scale wake location, related to wake thickness

τ normalized skin friction in laminar study; also Reynolds stress in turbulent problem

τ_w skin friction

ψ normalized stream function in computational plane

Ψ stream function

ω relaxation parameter

Superscripts:

* dimensional quantity

+	denotes wall-layer variable in turbulent analysis
^	denotes blending-layer variable in turbulent analysis
'	denotes differentiation with respect to indicated variable and perturbation quantity in turbulent flow

Subscripts:

B	bottom surface of airfoil
BL	perturbation quantity arising from upstream boundary layer in turbulent analysis
e	local quantity evaluated at edge of boundary layer
inv	perturbation quantity arising from outer inviscid flow in turbulent analysis
T	top surface of airfoil
TE	quantity evaluated at trailing edge, $X = 0$

THE LAMINAR-FLOW PROBLEM

Problems of laminar flow at large Reynolds numbers are usually analyzed by a combination of inviscid-flow and boundary-layer techniques. This approach is based on asymptotic expansions of the complete Navier-Stokes equations in the limit of Reynolds numbers approaching infinity. The inviscid and boundary-layer equations arise as the basic equations governing the leading approximation in the outer and inner regions, respectively. This approach leads to accurate and useful solutions of viscous-flow problems in many instances and has tended to dominate the history of fluid mechanics. However, in spite of its central role in fluid flows, the underlying structure of the asymptotic expansions are only relatively well understood for flows that are not separated and for geometries that are smooth.

It is well known that the inviscid and boundary-layer descriptions break down near separation points or near singular points of the geometry, such as sharp leading edges, corners, and trailing edges. A comprehensive review of these matters, including a discussion of higher order approximations, has been given by Van Dyke (ref. 19) and Stewartson (ref. 20).

In the trailing-edge problem, the nonuniformity of the basic expansions is caused jointly by a discontinuity in the surface boundary conditions at the trailing edge and by a singularity in the inviscid solution at the trailing edge of a lifting airfoil. The discontinuity in boundary conditions leads to a singularity in the boundary-layer solution at the trailing edge that is described by Goldstein's near wake solution (ref. 21). Goldstein's solution shows that the displacement surface develops a sharp corner with a vertical tangent on the downstream side of the trailing edge, as illustrated in figure 1. Goldberg and Cheng (ref. 22) have examined the second-order inviscid solution over a finite-length flat plate at zero incidence and have demonstrated that the inviscid flow over this displacement surface is singular, with the induced pressures approaching plus (minus) infinity on the downstream (upstream) side of the trailing edge.

The inviscid solution for subsonic flow near the trailing edge of a cusped airfoil at angle of attack exhibits a square-root singularity in the surface pressure distribution, as sketched in figure 1. The surface pressure is bounded but the pressure gradients are unbounded as the trailing edge is approached. The singular pressure gradients lead to singularities in the boundary-layer solution and to breakdown of the basic asymptotic expansions.

There have been numerous attempts to correct these defects and to develop an asymptotic theory that is uniformly valid at trailing edges, but for the most part, these were completely unsuccessful. It was only in the recent work of Stewartson (ref. 1) and, independently, Messiter (ref. 2) that a correct and rational treatment of the flow near trailing edges was given. In these works it was shown that the flow develops a characteristic multilayer structure near trailing edges that also arises in many other laminar interaction problems and which is referred to by Stewartson as a triple-deck model. A general discussion of viscous problems involving triple-deck structure is found in the recent review by Stewartson in reference 20.

The Triple-Deck Formulation

Stewartson and Messiter presented a rational treatment for the flow near a trailing edge. By using the method of matched asymptotic expansions, these investigators have shown that solutions of the Navier-Stokes equations near the trailing edge can be developed in asymptotic series in the limit of large Reynolds numbers. The solutions are cast in terms of a fundamental small parameter ϵ given in terms of the Reynolds number

$$\epsilon = R^{-1/8} \tag{1}$$

where R is the Reynolds number based on the length of the plate and the constant flow velocity far from the plate. Stewartson and Messiter considered the idealized case of incompressible flow over a finite flat plate at zero incidence. The theory was extended

to angle of attack by Brown and Stewartson in reference 3 for angles of attack α^* on the order of $\epsilon^{1/2}$. Although the theory of references 1 to 3 was developed for incompressible flow over finite flat plates, the basic theory is applicable to more general airfoils provided the airfoil is closely approximated by a flat plate near the trailing edge. For example, this requires the trailing-edge angle of an airfoil with thickness to be less than $0(\epsilon^2)$. The equations for the leading approximation are also applicable to compressible flows provided the Mach number of the inviscid solution is not near one in the trailing-edge region. In these cases compressibility effects enter only through a scale transformation of dependent and independent variables as given in references 3 and 20.

The structure of the triple-deck region is sketched in figure 2. The flow upstream and downstream of the triple-deck region is governed by standard inviscid and boundary-layer equations. The leading term in the outer inviscid region is given by constant uniform flow, while the solution in the upstream boundary layer is given by the Blasius solution and in the downstream wake by a modified Goldstein near wake solution, as described in reference 3. In the intermediate region between the Blasius and Goldstein region, the flow develops the multilayer structure sketched in figure 2. The ratio of the length scale of each region to the length of the plate L is also indicated in the figure. The streamwise length scale is $0(\epsilon^3)$, which is an order of magnitude larger than a boundary-layer thickness. Viscous effects are important only in the lower deck where the solution is governed by classical (incompressible) boundary-layer equations. Both pressure and viscous forces are negligible in the main deck to lowest order. The main role of the essentially passive main deck is to transmit flow deflections generated by the sublayer to the outer edge of the boundary layer. These flow deflections provide an inner boundary condition for the solution in the upper deck which is governed by inviscid small-disturbance equations. The solution in the inviscid upper deck is governed by elliptic partial differential equations which provide for the long upstream influence that was missed in many previous theories.

From the preceding discussion, it can be seen that the triple-deck formulation leads to a description of the flow as an interaction between the outer inviscid stream and the displacement thickness generated by the sublayer. The solution in the inviscid upper deck can be reduced to an integral relationship between the surface pressure and the flow deflection generated by the sublayer.

Solution of the triple-deck problem is thus reduced to that of determining solutions to the boundary-layer equations valid in the sublayer. These solutions must match the rotational flow in the main deck and must result in a displacement thickness and pressure distribution that satisfies the linear integral relationship arising from the outer solution.

The notation employed in references 1 to 3 and 20 varies. Here the notation employed by Stewartson in reference 1 will be followed with some exceptions. Physical

quantities are denoted by an asterisk, free-stream quantities by the subscript ∞, and the plate length by L. The quantities x^* and y^* are Cartesian coordinates parallel and transverse, respectively, to the plate with origin at the trailing edge, u^* and v^* are velocity components in the x^*- and y^*-directions, respectively, p^* is the pressure, ρ the density, α^* the angle of attack, and λ is a constant, equal to 0.33206, associated with the Blasius solution for the wall shear stress. Nondimensional variables for the lower deck are given by

$$\left.\begin{aligned} X &= \lambda^{5/4}x^*/\epsilon^3 L & Z &= \lambda^{3/4}y^*/\epsilon^5 L \\ U &= u^*/\epsilon\lambda^{1/4}U_\infty & V &= v^*/\epsilon^3\lambda^{3/4}U_\infty \\ P &= (p^* - p_\infty)/\epsilon^2\lambda^{1/2}\rho U_\infty^2 & \alpha &= \alpha^*/\epsilon^{1/2}\lambda^{9/8} \end{aligned}\right\} \tag{2}$$

(These scalings are for incompressible flow; for compressible flow, see refs. 3 and 20.) The Reynolds number R is given by $U_\infty L/\nu$, where ν is the kinematic viscosity coefficient.

For future reference, the solution for incompressible, inviscid flow over a flat plate of length L at incidence α^* is given by (for $y^* = 0$)

$$v^* = 0 \qquad u^* = U_\infty - U_\infty\alpha^* \frac{x^* + B}{\left[(-x^*)(L + x^*)\right]^{1/2}} \operatorname{sgn} y^* \qquad (-L < x^* < 0) \tag{3a}$$

$$u^* = U_\infty \qquad v^* = U_\infty\alpha^* \frac{x^* + B}{x^*(L + x^*)^{1/2}} \qquad (0 < x^*) \tag{3b}$$

The lift coefficient C_L corresponding to the solution is given by

$$C_L = 2\pi\alpha^*\left(1 - \frac{2B}{L}\right) \tag{4}$$

where B is a constant to be determined. The value of the constant B, determined by the Kutta condition applied to the trailing edge, would be zero. Here, however, the trailing-edge interaction leads to a nonzero value which gives a viscous correction to the lift coefficient. In reference 3 it was shown that this constant is $O(\epsilon^3 L)$ which leads to a viscous correction to the lift that is $O(\epsilon^3)$. A nondimensional circulation constant a_1 is introduced according to the definition

$$a_1 = \frac{B\lambda^{5/4}}{\epsilon^3 L} \tag{5}$$

The boundary-layer equations governing the flow in the lower deck are written in the form

$$\frac{\partial U}{\partial X} + \frac{\partial V}{\partial Z} = 0 \tag{6}$$

$$U \frac{\partial U}{\partial X} + V \frac{\partial U}{\partial Z} = - \frac{dP}{dX} + \frac{\partial^2 U}{\partial Z^2} \tag{7}$$

where the pressure P is a function of X alone.

Equations (6) and (7) are to be solved subject to the following boundary conditions:

$$U \to |Z| + \ldots \qquad (X \to -\infty) \tag{8a}$$

$$U = V = 0 \qquad (Z = 0;\ X < 0) \tag{8b}$$

$$P_T(X) = P_B(X) \qquad (X \geq 0) \tag{8c}$$

$$U \to |Z| + \ldots \longrightarrow \begin{cases} A_T(X) & (Z \to +\infty) \quad (8d) \\ -A_B(X) & (Z \to -\infty) \quad (8e) \end{cases}$$

where $P_T(X)$ and $P_B(X)$ are the pressures on the top and bottom of the X-axis, respectively, and $A_T(X)$ and $A_B(X)$ are perturbations of the displacement thickness from the undisturbed Blasius value at the trailing edge.

Finally, the pressure distribution must satisfy the following asymptotic condition in order to match the upstream inviscid solution

$$P_{T,B} \to -\alpha\sqrt{-X}\ \operatorname{sgn} Z \qquad (X \to -\infty) \tag{9}$$

where the subscript T,B is introduced for convenience to represent either the top of the bottom and $\operatorname{sgn} Z$ should be taken as plus for $Z > 0$ and minus for $Z < 0$. The pressure should decay to zero for $Z \to +\infty$ in order to match the Goldstein solution downstream.

Equation (8a) is a requirement that the velocity profile match to the inner portion of the Blasius solution far upstream. Equation (8c) follows from the requirement that the pressure be continuous across the wake. The application of this condition at the trailing edge ($X = 0$) is equivalent to the Kutta condition and serves to determine the constant a_1 defined by equation (5) and, therefore, the viscous correction to the lift coefficient.

Solution of the inviscid flow equations in the upper deck leads to the following integral relationship between the functions $A_{T,B}(X)$ and $P_{T,B}(X)$:

$$\frac{dA_T(X)}{dX} = -\frac{1}{\pi} \fint_{-\infty}^{+\infty} \frac{P_T(X_1)}{X - X_1} dX_1 \tag{10a}$$

$$\frac{dA_B(X)}{dX} = +\frac{1}{\pi} \fint_{-\infty}^{+\infty} \frac{P_B(X_1)}{X - X_1} dX_1 \tag{10b}$$

where the double slash on the integral sign means that Hadamard "finite part" of the divergent integral is to be taken. The integrals in equations (10) do not converge in the ordinary sense because of the behavior of the pressure for large negative X indicated in equation (9). A form more suitable for computation is given in the numerical methods section. Equations (10) are an inversion of the relationships given in reference 3 and are in a form that is most suitable for the numerical procedures used in the present investigation.

The preceding formulation indicates that to solve the triple-deck problem, the boundary-layer equations must be integrated subject to the vortical outer boundary conditions given by equations (8d) and (8e). The vorticity arises from the boundary-layer solution valid in the upstream flow. The upstream vorticity leads to additional algebraically growing terms in equations (8d) and (8e), as will be discussed later.

The pressure and displacement functions appearing in the boundary-layer equations and boundary conditions are unknown and must be determined as part of the solution of the boundary-layer equations such that the linear relation given in equations (10) is satisfied. The form of the pressure for large negative X is given by

$$P_{T,B} = \left(-\alpha\sqrt{-X} + \alpha a_1/\sqrt{-X} + \ldots\right) \operatorname{sgn} Z \tag{11}$$

where a_1 is related to the lift coefficient by equations (4) and (5). The lift coefficient can be obtained by solving the boundary-layer equations and extracting the constant a_1 from the expansion given in equation (11).

Asymptotic Properties of the Triple Deck

Equations (4) to (11) provide a complete formulation of the triple-deck problem. Useful asymptotic results were provided in references 1 to 3 and are extended and summarized in the following. (Corrections to a number of the signs are incorporated; see also ref. 6.)

For $X \to -\infty$, the solution must approach the perturbed Blasius solution and have the form

$$U = |Z| + 1.784|X|^{-1}F_1'(\eta) + \alpha|X|^{1/6}H_1'(\eta)\,\mathrm{sgn}\,Z + \alpha^2 H_2'(\eta) + \alpha^3|X|^{-1/6}H_3'(\eta)\,\mathrm{sgn}\,Z + \ldots \tag{12a}$$

and

$$\eta = \frac{|Z|}{3|2X|^{1/3}} \tag{12b}$$

where primes denote differentiation with respect to η. The similarity functions $F_1(\eta)$, $H_1(\eta)$, $H_2(\eta)$, and $H_3(\eta)$ satisfy ordinary differential equations given in references 1 and 3. The differential equations, boundary conditions, and asymptotic behavior required in the present work are listed in the appendix.

Other results for $X \to -\infty$ are

$$P(X) = -0.3433|X|^{-2/3} - 0.6867b_1|X|^{-5/3} - 0.0816X^{-2}\ln|X| + \frac{d_1}{|X|^2} + \ldots$$
$$- \alpha\left(|X|^{1/2} - a_1|X|^{-1/2} + 0.2368|X|^{-5/6} + \ldots\right)\mathrm{sgn}\,Z + \ldots \tag{13a}$$

$$A(X) = 0.3265|X|^{-1} + \alpha C_{12}|X|^{1/6}\,\mathrm{sgn}\,Z - \alpha^2 C_{21}\left(\frac{1}{3}\ln|X| + \ln K\right) + \alpha^2(C_{21} + C_{22})$$
$$+ \alpha^3 C_{33}|X|^{-1/6}\,\mathrm{sgn}\,Z + \ldots \tag{13b}$$

$$\left.\frac{\partial U}{\partial Z}\right|_{Z=0} = 1 + 0.3106|X|^{-4/3} - \alpha(2.1539)|X|^{-1/6}\,\mathrm{sgn}\,Z + \ldots \tag{13c}$$

where K and the C_{ij}'s are known constants listed in the appendix.

For $X \to +\infty$ the velocity profile approaches the inner solution of Goldstein's near wake solution. The behavior of $P(X)$, $A_{T,B}(X)$, and $U(X,0)$ are given by

$$P(X) = 0.1717X^{-2/3} + 0.3433b_1X^{-5/3} - 0.0816X^{-2}\ln X + d_1X^{-2} + \ldots \tag{14a}$$

$$A_{T,B}(X) = 1.416\left(\frac{1}{4}X\right)^{1/3}\mathrm{sgn}\,Z + 1.416\left(\frac{1}{4}\right)^{1/3}b_1X^{-2/3}\,\mathrm{sgn}\,Z - \alpha\left[\frac{2}{3}X^{3/2} + 2a_1X^{1/2}\right.$$
$$\left. - \left(\frac{1}{6}\right)^{1/6}2^{3/2}\left(-\frac{1}{3}\right)!X^{1/6}\right] + \ldots \tag{14b}$$

$$U(X,0) = 1.611X^{1/3} + 1.611b_1X^{-2/3} + 0.052X^{-1} + \ldots \tag{14c}$$

The solution of the triple-deck equations develops a singularity at the trailing edge that is described by the Goldstein solution (ref. 21) for $\alpha = 0$ and by the Hakkinen-Rott near wake solution (ref. 23) for $\alpha \neq 0$. In both cases the velocity profile has the following form for X and $Z \to 0$

$$U = \frac{1}{3}\left(\frac{1}{4}X\right)^{1/3} G_0'(\eta) \tag{15}$$

where η is given by equation (12b) and G_0 satisfies an ordinary differential equation studied in reference 23 and listed in the appendix.

For zero incidence, the local solution for $X \to 0$ is given as follows:

For $X < 0$,

$$P = P_{TE} + P'_{TE}X + \left(P_2 \ln|X| + P_3\right)X^2 + \ldots \tag{16a}$$

$$A = A_{TE} + A'_{TE}X - \left(3^{3/2}/5\right)C_0|X|^{5/3} + \frac{1}{2}A_1^-X^2 + \ldots \tag{16b}$$

$$\left.\frac{\partial U}{\partial Z}\right|_{Z=0} = \lambda_1 \tag{16c}$$

and for $X > 0$,

$$P = P_{TE} + \frac{3}{2}C_0X^{2/3} + P_1X + \ldots \tag{17a}$$

$$A = A_{TE} + A'_{TE}X + \left(3^{3/2}/10\right)C_0X^{5/3} + \frac{1}{2}A_1^+X^2 + \ldots \tag{17b}$$

$$U = 1.4061C_0^{1/2}X^{1/3} + \ldots \tag{17c}$$

$$C_0 = 0.4089\lambda_1^{4/3} \tag{17d}$$

The local solution for $X \to 0$ when $\alpha \neq 0$ is slightly more complicated for $X < 0$. Equation (16a) now takes the form

$$P_{T,B} = P_{TE} + \left(P'_{TE}\right)_{T,B}X + \left[\left(P_2\right)_{T,B} + \left(P_3\right)_{T,B}X\right]X^{-2}\ln|X| + \ldots \qquad (18a)$$

Equation (16b) has different expressions for A_T and A_B

$$A_T = \left(A_{TE}\right)_T + \left(A'_{TE}\right)_T X - \left(3^{3/2}/5\right)C_o|X|^{5/3} + \tfrac{1}{2}\left(A_1^-\right)_T X^2 + \ldots \qquad (18b)$$

$$A_B = \left(A_{TE}\right)_B + \left(A'_{TE}\right)_B X + \left(3^{3/2}/5\right)C_o|X|^{5/3} + \tfrac{1}{2}\left(A_1^-\right)_B X^2 + \ldots \qquad (18c)$$

and

$$\left.\frac{\partial U}{\partial Z}\right|_{Z=0^+,X=0} = \lambda_{1,T} \qquad \left.\frac{\partial U}{\partial Z}\right|_{Z=0^-,X=0} = \lambda_{1,B} \qquad (18d)$$

For $X > 0$, equation (17a) has the same form. Equation (17b) becomes

$$A_T = \left(A_{TE}\right)_T + \left(A'_{TE}\right)_T X + \left(3^{3/2}/10\right)C_o X^{5/3} + \tfrac{1}{2}\left(A_1^+\right)_T X^2 + \ldots \qquad (18e)$$

$$A_B = \left(A_{TE}\right)_B + \left(A'_{TE}\right)_B X - \left(3^{3/2}/10\right)C_o X^{5/3} + \tfrac{1}{2}\left(A_1^+\right)_B X^2 + \ldots \qquad (18f)$$

and equations (17c) and (17d) assume the forms, respectively,

$$U = \gamma C_o^{1/2} X^{1/3} + \ldots \qquad (18g)$$

$$C_o = C_o\left(\lambda_{1,T}\lambda_{1,B}\right) \qquad (18h)$$

where γ and C_o are now functions of $\lambda_{1,T}$ and $\lambda_{1,B}$ and are determined by solving the merging asymmetrical shear flow problems of Hakkinen and Rott.

The two sets of constants (a_1, b_1, d_1) and $\left(P_{TE}, P'_{TE}, P_2, P_3, A_{TE}, A'_{TE}, A_1^-, A_1^+, \text{ and } \lambda_1\right)_{T,B}$ appearing in the preceding expansions are not determined by the local solution. The first set relates to the far-field solution while the second set relates to the local solution near the trailing edge. Values for all but d_1 have been estimated for $\alpha = 0$ by fitting the asymptotic forms to the numerical solutions obtained in the present study.

For future reference the behavior of the velocity profile for large Z and fixed X is given as

$$U = |Z| + \left(\alpha C_{11}/K^{1/2}\right)|Z|^{1/2}\,\mathrm{sgn}\,Z + \alpha^2 C_{21}\ln|Z| + \left(\alpha^3 C_{31}K^{1/2}/2\right)\left(|Z|^{-1/2}\ln|Z|\right)\mathrm{sgn}\,Z$$

$$+ A_{T,B}\,\mathrm{sgn}\,Z + \left\{\left(\alpha C_{11}/2K^{1/2}\right)A_{T,B} + \left(\alpha^3/2K^{1/2}\right)\left[C_{11}(C_{21} - C_{22})\right.\right.$$

$$\left.\left. + KC_{34}\right]\mathrm{sgn}\,Z\right\}|Z|^{-1/2} - a_2|Z|^{-3} + \ldots \tag{19a}$$

The constants C_{ij} and K are listed in the appendix and

$$a_2 = 1.784\left[\frac{\Gamma(4/3)}{3^{25/6}\left(-\frac{1}{3}\right)!}\right] \tag{19b}$$

The preceding expansion was obtained by expanding the solution of the boundary-layer equations for large Z and matching to the asymptotic expansion of the initial profile defined by equations (12). (See results in appendix.) This matching enabled the set of arbitrary constants appearing in equations (10) to be identified with the constants given in the appendix. Equations (19) are used to set the far-field boundary conditions in a finite difference procedure described in the following section.

THE NUMERICAL METHOD

The boundary-value problem to be solved for the trailing-edge solution is illustrated in figure 3. The boundary-layer equations must be solved such that the solution matches the Blasius solution far upstream and the Goldstein solution far downstream. No-slip conditions must be satisfied on both sides of the flat plate and asymptotic boundary conditions must be satisfied on each side of the boundary layer and wake for $|Z| \to \infty$. The pressure gradient appearing in the momentum equation and the displacement functions $A_T(X)$ and $A_B(X)$ appearing in the outer boundary condition must be determined such that they satisfy the linear integral relationship imposed by the outer inviscid solution. In addition, the condition that the pressure decays to zero as $X \to +\infty$ must be imposed in order to match the Goldstein solution. In the present approach, a fixed point iteration between the inviscid and boundary-layer equations is employed. The principal difficulties in the numerical solution of the boundary-layer equations are due to a singularity at the trailing edge and to a slow algebraic decay of the solution for $|X|$ and $|Z| \to \infty$. These problems are treated by using asymptotic solutions to set the far-field boundary conditions at finite distances and to describe the singular solution near the trailing edge. A highly nonuniform mesh distribution is also employed to obtain proper resolution near the trailing edge and to allow for the slow decay of the solution in the far field.

The boundary-layer equations are solved by the Keller-Cebeci (refs. 4 and 5) finite-difference scheme for parabolic partial differential equations. This method is well suited to the present problem since it is second-order accurate, unconditionally stable, and permits highly nonuniform mesh distributions. The Hilbert transformations in equations (10), which provide the inviscid solution, are evaluated by special quadrature formula on the same mesh distribution employed in the boundary-layer calculation. This avoids the need to interpolate between the inviscid and viscous solutions. The resulting computation has uniform second-order accuracy, including the far field and the singular point at the trailing edge.

The Iteration Scheme

The iteration procedure is indicated in figure 3. The path of the iteration is in a direction inverse to that usually employed in similar viscous interaction problems. Here, the displacement functions $A_{T,B}(X)$ are obtained from solutions of the inviscid equations (i.e., eqs. (10)) with the pressure distribution prescribed. The pressure distributions $P_{T,B}(X)$ are determined from solutions of the boundary-layer equations. Since the unknown pressure gradient appears in these equations, an additional relation is needed to complete their solution. This is supplied by the previous evaluation of the displacement function $A_{T,B}(X)$ which provides an outer boundary condition for the solution of the viscous equations. This indirect iteration sequence is followed because it provides a convenient and simple treatment of the trailing-edge singularity. In a conventional iteration, the solution of the boundary-layer equations for a prescribed pressure distribution results in a discontinuity in the slope of the displacement function at the trailing edge. This, in turn, leads to unbounded pressures in the inviscid solution and to divergence of the iteration sequence.

The iteration starts with estimated pressure distributions $P_T(X)$ and $P_B(X)$ which appear in the integrands of the Hilbert integrals. The integrals are evaluated by a second-order-accurate quadrature scheme to yield expressions for dA_T/dX and dA_B/dX. The displacement functions A_T and A_B are then obtained by integration using a trapezoidal rule with initial values determined from the upstream asymptotic expansions given in equation (13b). This half-cycle yields an intermediate solution for the displacement functions $A_{T,B}(X)$.

In the next half-cycle the boundary-layer equations are integrated. A minor difficulty arises because of the presence of the unknown pressure gradient in the differential equations. To deal with this problem the momentum equation is differentiated with respect to Z. This eliminates the pressure but increases the order of the equations from a third- to a fourth-order system of partial differential equations. An additional boundary condition is required to close the system. This is supplied by using the known functions

$A_{T,B}(X)$ in the asymptotic expansion given in equations (19) to yield a condition on the streamwise velocity component as $|Z| \to \infty$. This condition and the conditions that the shear stress approach one for $|Z| \to \infty$ and that both velocity components vanish on the plate result in a well-posed problem. A finite-difference scheme, described in the next subsection, is employed to integrate the boundary-layer equations starting from an initial station far upstream of the trailing edge. Profiles at the initial station are determined from the first five terms of the asymptotic solution given in equations (12). The boundary-layer equations are solved by marching downstream to the trailing edge on the top and bottom of the plate independently. A local solution describing the singular behavior at the trailing edge is obtained by numerically solving the similarity equations, first considered by Hakkinen and Rott in reference 23. The similarity solution is used to construct a "composite" profile across the sublayer at a station just downstream of the trailing edge. The solution is then marched downstream, employing two boundary conditions on each side of the wake, as indicated in figure 3. After completion of the sweep, the pressure gradient is determined from the momentum equation evaluated on the X-axis at $Z = 0$. The pressure is then computed from a trapezoidal integration of the gradient. Two arbitrary constants of integration, the trailing-edge pressure and the circulation constant a_1 (see eq. (11)) are evaluated by matching the pressure to the upstream data and by requiring the pressure difference to vanish at the trailing edge.

The boundary-layer solution cannot be continued downstream to very large distances because of the appearance of a growing solution $P = P_G X^{2/3}$ for $X \to +\infty$. The solution is induced by a wake thickness distribution $\frac{1}{2}(A_T + A_B) \approx A_G X^{1/3}$ which appears in the outer boundary conditions. The constant P_G vanishes and the unwanted solution is excluded if the constant A_G is exactly equal to the Goldstein value $(A_G = 0.892\ldots)$. However, because of the finite arithmetic carried in the computer, this solution cannot be excluded from the numerical solution and it eventually dominates the far-field behavior. Consequently, the boundary-layer solution must be terminated at a station $X = X_p$ that is taken to be upstream of the region where the spurious growing solution starts to dominate. This raises a minor problem, since a solution for the pressure distribution $P(X)$ along the entire X-axis must be supplied for the evaluation of the Hilbert integral. This is easily remedied by using an analytic expression to represent the pressure distribution downstream of the terminal point $X = X_p$. In the computer program an expression is employed that matches both the pressure and pressure gradient at $X = X_p$ and has the correct asymptotic behavior for $X \to +\infty$. Numerical experiments, to be discussed at the end of the section, have indicated that this procedure provides a smooth continuation of the solution downstream of $X = X_p$ and has a negligible effect on the upstream solution.

This half-cycle results in a complete solution for the pressure distribution which can be substituted into the Hilbert integral to obtain new estimates for the displacement

functions. The integration is continued until the solution converges to a required tolerance. As usually required in this type of problem, the solution must be underrelaxed in order to obtain convergence.

The value of $P(X)$ is relaxed according to the formula

$$P(X) = \omega P(X)_{new} + (1 - \omega)P(X)_{old}$$

where P_{old} is the pressure at the start of the boundary-layer computation, P_{new} is the pressure computed at the most recent sweep, and ω is a relaxation parameter ($\omega < 1$) that is adjusted to obtain convergence. In the present scheme it is found that the value of ω must be reduced as the extent of the streamwise interval is increased in the downstream direction. Accordingly, the following strategy is employed. The calculation starts with a given relaxation parameter small enough to obtain convergence with an initial choice of $X_P = 3$. The solution is converged with these choices, the terminal point is moved further downstream, ω is reduced, and the calculations repeated. Converged results have been obtained starting with values of $\omega = 0.15$ and $X_P = 3$ and ending with $\omega = 0.02$ and $X_P = 20.791$.

Solution of the Boundary-Layer Equations

The boundary-layer equations are solved by the Keller-Cebeci "box" scheme (refs. 4 and 5). The unknown pressure gradient is eliminated from the boundary-layer equations by application of a Z-derivative to the momentum equations. A stream function Ψ is introduced and the boundary-layer equations are written as a system of four first-order partial differential equations. The wake thickness and centerline position become unbounded as $X \to \infty$. To control the wake growth the Z-coordinate is scaled such that wake position is bounded in the computational plane. A scale transformation is defined in terms of two parameters $\sigma(X)$ and $\theta(X)$ by the following relation:

$$y = \frac{Z - \theta(X)}{\sigma(X)} \tag{20}$$

where y is a scaled coordinate in the direction normal to the plate and the functions $\sigma(X)$ and $\theta(X)$ are given in terms of $A_{T,B}(X)$ by

$$\sigma(X) = \begin{cases} \sigma_0 & (X < L_1) \quad (21a) \\ \sigma_0 + \frac{1}{2}\left[A_T(X) - A_B(X)\right] - \frac{1}{2}\left[A_T(L_1) - A_B(L_1)\right] & (X \geq L_1) \quad (21b) \end{cases}$$

$$\theta(X) = -\frac{1}{2}\left[A_T(X) + A_B(X)\right] + \frac{1}{2}\left[A_T(L_1) + A_B(L_1)\right] \qquad (X \geq L_1) \qquad (22)$$

where σ_o is a constant scale parameter and L_1 is a small positive number that identifies the streamwise station where the wake solution is initialized. The functions $\sigma(X)$ and $\theta(X)$ control the wake thickness and position, respectively. The choice of $\theta(X)$ was previously discussed in reference 3. This scaling minimizes the variations of wake location in the far field and as a result, the computations can be carried out with fixed outer boundaries in the y-plane. In addition the coordinates approach similarity variables appropriate to the Goldstein solution for $X \to +\infty$. Scaled dependent variables are also introduced according to the relations

$$\Psi = \sigma(X)^2 \psi(X,y) \tag{23a}$$

$$U = \sigma(X)\, u(X,y) \tag{23b}$$

$$\tau = \tau(X,y) \tag{23c}$$

$$D = \sigma(X)^{-1} d(X,y) \tag{23d}$$

where Ψ, U, τ, and D are, respectively, the stream function, streamwise velocity component, shear stress, and derivative of shear stress with respect to Z $\left(\text{i.e., } D = \frac{\partial \tau}{\partial Z}\right)$ and where ψ, u, τ, and d are, respectively, scaled versions of the stream function, streamwise velocity component, shear stress, and derivative of shear stress with respect to Z. With these transformations and with the elimination of the pressure gradient, the governing equations can be written in the form

$$\frac{\partial \psi}{\partial y} = u \tag{24a}$$

$$\frac{\partial u}{\partial y} = \tau \tag{24b}$$

$$\frac{\partial \tau}{\partial y} = d \tag{24c}$$

$$\frac{\partial d}{\partial y} = \sigma(X)^3 \left(u \frac{\partial \tau}{\partial X} - d \frac{\partial \psi}{\partial X} \right) - 2\sigma(X)^2 \sigma'(X) \psi d \tag{24d}$$

In this formulation the boundary condition on V given in equation (8b) is replaced by the equivalent condition on the stream function

$$\psi = 0 \qquad (y = 0;\ X < 0) \tag{25}$$

A general, nonuniform rectangular mesh is introduced and equations (24) are differenced according to the box scheme along the lines indicated in figure 4. The X-columns

are labeled by an index I and the horizontal rows by an index J starting from J = 1 on the lower boundary and continuing to $J = J_P$ on the upper boundary, where J_P is the number of points in the y-mesh on the top of the plate. The first three equations do not involve X-derivatives. These are central differenced about a midpoint of a y-interval on the most forward marching column. Equation (24d), which is nonlinear and involves derivatives in both directions, is central differenced about the midpoint of the box, as indicated in figure 4. The nonlinear coefficients are evaluated as four point averages at the midpoint of the box. This difference approximation leads to a nonlinear set of difference equations for the vector unknowns $(\psi,u,\tau,d)_J$ along the column I + 1. The difference approximation is second-order accurate and implicit since it couples all the unknowns along the I + 1 column.

The boundary conditions along the plate involve the specification of the two components $\psi(X_{I,0})$ and $u(X_{I,0})$ for $X < 0$. Outer boundary conditions are imposed on the vector components u and d. The conditions are given in the form of a ratio at the outer two points of the mesh J_P and J_{P-1}. The ratios for the conditions on top of the plate are computed from the asymptotic far-field expansion given in equations (19) as follows:

$$\frac{\sigma(X)u_{J_P} - R_{11}\left(Z_{J_P},X\right) - A_T(X)}{\sigma(X)u_{J_{P-1}} - R_{11}\left(Z_{J_{P-1}},X\right) - A_T(X)} = \frac{R_{12}\left(Z_{J_P},X\right)}{R_{12}\left(Z_{J_{P-1}},X\right)} \tag{26a}$$

$$\frac{d_{J_P}\Big/\sigma(X) + R_{21}\left(Z_{J_P},X\right)}{d_{J_{P-1}}\Big/\sigma(X) + R_{21}\left(Z_{J_{P-1}},X\right)} = \frac{R_{22}\left(Z_{J_P},X\right)}{R_{22}\left(Z_{J_{P-1}},X\right)} \tag{26b}$$

where

$$R_{11}(Z,X) + Z + \frac{\alpha C_{11}}{K^{1/2}} Z^{1/2} + \alpha^2 C_{21} \ln Z + \alpha^3 \frac{C_{31}}{2} K^{1/2} Z^{-1/2} \ln Z \tag{27a}$$

$$R_{12}(Z,X) = \left\{\frac{\alpha C_{11}}{2K^{1/2}} A_T(X) + \frac{\alpha^3}{2K^{1/2}}\left[C_{11}(C_{21} - C_{22}) + KC_{34}\right]\right\} Z^{-1/2} - a_2 Z^{-3} \tag{27b}$$

$$R_{21}(Z,X) = \frac{\alpha C_{11}}{4K^{1/2}} Z^{-3/2} + \alpha^2 C_{21} Z^{-2} - \frac{3}{8}\alpha^3 K^{1/2} C_{31} Z^{-5/2} \ln Z \tag{28a}$$

$$R_{22}(Z,X) = \frac{3}{8K^{1/2}}\left[\alpha C_{11} A_T(X) + \alpha^3\left(-C_{11}C_{22} + KC_{34} - \frac{5}{3} C_{11}C_{21}\right)\right] Z^{-5/2} - 12 a_2 Z^{-5} \tag{28b}$$

where Z is related to the computational coordinate y by

$$Z = \theta(X) + \sigma(X)y \tag{29}$$

This procedure for satisfying the far-field boundary conditions was motivated by the work of Ackerberg and Phillips (ref. 24). Similar expressions are applied to the bottom boundary of the mesh. For the wake computations $(X \geq L_1)$, only the outer boundary conditions are to be satisfied and the expressions are identical to those of equations (26), (27), and (28).

The difference equations are solved by a Newton-Raphson technique. The nonlinear equations are linearized about a previous estimate to form a linear system of algebraic equations for the perturbation quantities $(\delta\psi, \delta u, \delta\tau, \delta d)_J^{I+1}$. The differential equations and boundary conditions result in a linear system that has a block tridiagonal form. In the present problem the main blocks are 4×4 square matrices. The equations are solved by an efficient Gaussian elimination technique as described in reference 5. The form of the outer boundary conditions given in equations (26) automatically falls into this block structure.

Solutions at the most recently computed station (e.g., station I in fig. 4) are employed as initial estimates. Quadratic convergence was observed to occur with these starting values. The iteration was continued until a convergence criterion based on the relative error was satisfied at all mesh points. The criterion

$$\frac{|\delta f(I+1,J)|}{|f(I+1,J) + \delta f(I+1,J)|} < \epsilon_1 \tag{30}$$

is employed, where f stands for any one of the dependent variables.

The calculation proceeds by marching in the X-direction starting from an initial station $X = L_0$. Initial profiles are determined from the asymptotic solution given in equations (12). The similarity functions $F_1(\eta)$, $H_1(\eta)$, $H_2(\eta)$, and $H_3(\eta)$ appearing in the asymptotic solutions are determined from a numerical integration of the two-point boundary-value problems formulated in the appendix. These solutions are obtained with the same subroutine employed in the marching calculation.

When the trailing edge $(X = 0)$ is reached, a composite solution is formed to describe the initial wake profile a short distance $(\Delta X = L_1)$ downstream of the trailing edge. The composite profile is obtained from a coordinate expansion for X and $Z \to 0$. It is written as the sum of an outer and inner solution less the "common part." The structure of the local solution is similar to Goldstein's near wake solution except for the presence of a singular, self-induced pressure gradient in the similarity equation. Solutions were first

obtained by Hakkinen and Rott in reference 23 and are further discussed in references 1 to 3 and 20. The wake initial profile is given by

$$U(L_1,Z) = U_T(0,Z) + \frac{1}{3}\left(\frac{1}{4}L_1\right)^{1/3} G_0'(\eta) - \lambda_{1,T}Z \qquad (Z > 0) \qquad (31)$$

$$U(L_1,Z) = U_B(0,Z) + \frac{1}{3}\left(\frac{1}{4}L_1\right)^{1/3} G_0'(\eta) - \lambda_{1,B}Z \qquad (Z < 0) \qquad (32)$$

where U_T and U_B are the velocity profiles at the trailing edge on the top and bottom of the plate, respectively, G_0' is the similarity function describing the "inner" Hakkinen-Rott solution, η is a similarity variable defined by equation (12b), and $\lambda_{1,T}$ and $\lambda_{1,B}$ are the skin-friction coefficients at the trailing edge. (See eq. (18d).) Profiles for the variables ψ, τ, and d can be formed in a similar manner. The function $G_0'(\eta)$ is determined as part of the solution by integrating the two-point boundary-value problem formulated in the appendix. The solution in the wake is then continued downstream, starting from the initial wake station $(X = L_1)$ and terminating at a station $(X = X_P)$ chosen at the start of the calculations, as discussed in the beginning of this section.

The pressure distribution is determined after completion of the forward sweep by integrating the streamwise momentum equation

$$\frac{dP}{dX} = \frac{d(X,0)}{\sigma(X)} + \sigma(X)^2\left[\tau(X,0)\frac{\partial\psi(X,0)}{\partial X} - u(X,0)\frac{\partial u(X,0)}{\partial X}\right] - \frac{u^2(X,0)}{2}\frac{d\sigma^2(X)}{dX} \qquad (33)$$

All quantities on the right side of equation (33) are known from the most recent sweep. Separate equations hold on the top and bottom of the plate. The pressure is determined by a simple trapezoidal integration

$$P_{T,B}(I+1) - P_{T,B}(I) = \left[X(I+1) - X(I)\right]\left(\frac{dP_{T,B}}{dX}\right)_{I+1/2} \qquad (34)$$

where the pressure gradient is evaluated by averaging equation (33) over the stations $X(I+1)$ and $X(I)$. Two constants of integration are required to complete the solutions given in equation (34). These are determined from the asymptotic solutions given in equation (13a), which give

$$P_T(X = L_0) = -\alpha\sqrt{|L_0|} + \frac{\alpha a_1}{\sqrt{|L_0|}} - \frac{0.3433}{|L_0|^{2/3}} - \frac{0.2368\alpha}{|L_0|^{5/6}} \qquad (35a)$$

$$P_B(X = L_0) = \alpha\sqrt{|L_0|} - \frac{\alpha a_1}{\sqrt{|L_0|}} - \frac{0.3433}{|L_0|^{2/3}} + \frac{0.2368\alpha}{|L_0|^{5/6}} \qquad (35b)$$

Note that these relations involve the unknown circulation constant a_1 which must be determined before the solution can be completed. The circulation constant a_1 is determined from a generalized Kutta condition as follows. By definition

$$\left.\begin{aligned} P_T(0) &= P_T(X = L_o) + \int_{L_o}^{0} \left(\frac{dP_T}{dX}\right) dX \\ P_B(0) &= P_B(X = L_o) + \int_{L_o}^{0} \left(\frac{dP_B}{dX}\right) dX \end{aligned}\right\} \tag{36}$$

If equations (35) are substituted into equations (36) and the Kutta condition that the pressure is continuous at the trailing edge (i.e., $P_T(0) = P_B(0)$) is imposed, the following relations are obtained:

$$P_T(0) = P_B(0) = -\frac{0.3433}{|L_o|^{2/3}} + \frac{1}{2}\int_{L_o}^{0} \left(\frac{dP_T}{dX} + \frac{dP_B}{dX}\right) dX \tag{37a}$$

$$a_1 = |L_o| + \frac{0.2368}{|L_o|^{1/3}} - \frac{\sqrt{|L_o|}}{2\alpha}\int_{L_o}^{0} \left(\frac{dP_T}{dX} - \frac{dP_B}{dX}\right) dX \tag{37b}$$

Equations (37) should be interpreted as asymptotic relations valid for $L_o \to -\infty$. The present results indicate that the solution is not overly sensitive to the magnitude of L_o and that a_1 can be evaluated to two decimal places for $L_o = -17$. Equation (37a) has been employed in conjunction with equation (34) to determine the surface pressure by sweeping equation (34) from the trailing edge.

The differential equations are differenced in Cartesian coordinates on a nonuniform mesh. The grid-point distribution is determined from simple transformations that map a uniform grid to a nonuniform grid. The parameters of the mapping are adjusted to concentrate mesh points in regions of large gradients that occur on the axis ($y = 0$) and at the trailing edge ($X = 0$). The distribution of y-grid points is given as follows for the upper half-plane. The mesh points in the lower half-plane are obtained by reflection about the X-axis.

On the plate side ($X < 0$) the $y(J)$ distribution is defined by the relations

$$y(J) = \frac{\zeta y_M}{1 + B_p(1 - \zeta)} \tag{38a}$$

$$B_P = \frac{J_P - 1}{K_1}\left(\frac{1 - K_1}{J_P - 2}\right) \tag{38b}$$

and

$$\zeta = \frac{J - 1}{J_P - 1} \qquad \left(1 \leq J \leq J_P\right) \tag{38c}$$

where y_M is the upper boundary of the computational domain, J is a running index, and K_1 is a parameter employed to control the relative spacing of the increments. Equations (38) reduce to a uniform mesh for $K_1 = 1$ and to a nonuniform mesh with a concentration of mesh points near the wall for $K_1 < 1$.

On the wake side of the field, a two-piece grid consisting of a fine uniform grid was employed near the axis, and a stretched grid was used in the outer part of the wake. The grid for $X > 0$ is defined by the following relations. For the inner region

$$y(J) = y_{inner}\frac{J - 1}{J_{inner} - 1} \qquad \left(1 \leq J \leq J_{inner};\ 0 \leq y \leq y_{inner}\right) \tag{39a}$$

and for the outer region

$$y(J) = y_{inner} + \left(y_M - y_{inner}\right)\left[\frac{\zeta}{1 + B_P(1 - \zeta)}\right]\left[1 + K_2(1 - \zeta) + K_3(1 - \zeta)^2\right] \tag{39b}$$

where

$$\zeta = \frac{J_W - J}{J_W - J_{inner}} \qquad \left(J_{inner} < J \leq J_W;\ y_{inner} < y \leq y_M\right) \tag{39c}$$

where y_{inner} is the upper boundary of uniform mesh region, J is a running index, J_{inner} is the number of mesh points in the inner region, J_W is the total number of mesh points employed in the wake, and K_2 and K_3 are parameters that control the mesh distribution in the outer region. They are chosen such that (1) the mesh increment is continuous across the boundary between the inner and outer regions and (2) the outermost increment $y\left(J_W\right) - y\left(J_W - 1\right)$ is equal to the corresponding increment on the plate. The mesh distribution in the marching or X-direction is chosen to provide for a concentration of mesh points on the wake side of the trailing edge and for a gradual stretching in the far field for $X \to \pm\infty$.

On the plate side ($X < 0$) the following transformation is employed:

$$X(I) = L_0 \xi \left(\frac{1 - K_4}{1 - K_4 \xi} \right)^3 \tag{40a}$$

where

$$\xi = \frac{I_p - I}{I_p - 1} \qquad \left(1 \leqq I \leqq I_p;\ L_0 \leqq X \leqq 0\right) \tag{40b}$$

L_0 is the value of X at the initial station, I is a running index, I_p is the number of X-mesh points used on the plate, and K_4 is a parameter that controls the relative spacing of the mesh points on the plate. Equations (40) generate a uniform mesh for $K_4 = 0$ and a nonuniform mesh for $K_4 > 0$. A relation between K_4 and the minimum mesh increment Δ_1 is given by

$$K_4 = \frac{\left(I_p - 1\right) + \left(I_p - 1\right)\left[\Delta_1 \left(I_p - 1\right) / L_0\right]^{1/3}}{\left(I_p - 1\right) - \left[\Delta_1 \left(I_p - 1\right) / L_0\right]^{1/3}} \tag{41}$$

With equations (40) and (41), a mesh distribution can be generated with a specified minimum increment Δ_1 at the trailing edge that smoothly expands to the initial point $\left(X = L_0,\ I = 1\right)$.

The streamwise mesh distribution in the wake is given in three parts: a nonuniform region near the trailing edge that concentrates points near the origin, an intermediate region with a uniform mesh, and a nonuniform region with an expanding grid in the downstream direction. A good distribution is generated by the following relations:

$$X(I) = \frac{\Delta_2 \left(I - I_p\right)^3}{\left(I_1 - I_p\right)^2 - \left(I_1 - I_p - 1\right)^3} \qquad \left(I_p < I \leqq I_1\right) \tag{42a}$$

$$X(I) = X(I - 1) + \Delta_2 \qquad \left(I_1 < I \leqq I_2\right) \tag{42b}$$

$$X(I) = X\left(I_2\right) + \frac{\Delta_2 \left(I - I_3\right)}{\left[1 - K_5 \left(I - I_3\right)\right]^3} \qquad \left(I_2 \leqq I < I_3\right) \tag{42c}$$

and

$$K_5 = \left\{1 - \left[\frac{\Delta_2(I_3 + 1 - I_2)}{L_{max} - X(I_2)}\right]^{1/3}\right\}\left(\frac{1}{I_3 + 1 - I_2}\right) \tag{43}$$

where Δ_2 is a parameter that controls the first mesh increment in the wake, I_1, I_2, and I_3 are the values of the running index I that separate the three mesh regions, and L_{max} is the coordinate of the downstream boundary of the mesh. Note that I_3 is also equal to the total number of points used in the streamwise direction. Attention is called to the fact that L_{max} need not be equal to the terminal point of the boundary-layer calculation, $X = X_p$.

Evaluation of the Hilbert Integral

The most recent sweep of the boundary-layer equations provides updated solutions for the pressure distributions required for the evaluation of the Hilbert integrals given in equations (10). The main difficulties in the numerical evaluation of these integrals are associated with the infinite range of integration, the algebraic singularity in the integrand for $X \to -\infty$, the pole singularity at $X = X_1$, and the infinite pressure gradient for $X \to 0^+$.

The first two problems are treated by dividing the integration interval into a number of segments. The outer two segments contain the unbounded intervals $X \to +\infty$ and $X \to -\infty$. In these regions, the pressure distribution is approximated by the asymptotic expressions given in equations (13a), (13b), and (14a), and the integrals are evaluated in closed form. This reduces the numerical problem to one involving an integration over a finite range and also provides for a correct evaluation of the singular "finite part" integral for $X \to -\infty$. The remaining integrals are over a finite range and are evaluated by numerical quadrature using the mesh distribution employed in the boundary-layer calculation. Difficulties with the pole singularity are avoided by evaluating the integrals only at the midpoints of the integration intervals used in the quadrature. Excessive truncation error due to the singular pressure gradients near the trailing edge is avoided by using a special quadrature formula that accounts for this behavior. On the plate, the integration interval is split into two segments, $-\infty < X \leq L_0$ and $L_0 < X < 0$, while in the wake, $0 < X < L_1$, $L_1 < X < L_2$ and $L_2 < X < +\infty$. Note that segment boundaries L_1, L_2, and L_3 need not line up with the boundaries of the mesh defined by equations (42). With this division, the integrals can be expressed as the following summation

$$A'_{T,B}(X) = \frac{\alpha}{\pi} T_1 - \text{sgn } Z(T_2 + T_3 + \Lambda_{10} + \Lambda_{02} + \Lambda_{23}) \tag{44}$$

where the far-field expressions have been used to evaluate the integrands of the integrals T_1, T_2, and T_3 as follows:

$$T_1 = \int_{-\infty}^{L_o} \frac{\sqrt{-X_1}\,dX_1}{X - X_1} - a_1 \int_{-\infty}^{L_o} \frac{dX_1}{\sqrt{-X_1}(X - X_1)} + \frac{(-1/3)!}{\sqrt{3}(6)^{2/3}} \int_{-\infty}^{L_o} \frac{dX_1}{(-X)^{5/6}(X - X_1)} \tag{45a}$$

$$T_2 = -\frac{1.784}{3\sqrt{3}} \int_{-\infty}^{L_o} \frac{dX_1}{(-X)^{2/3}(X - X_1)} \tag{45b}$$

$$T_3 = \frac{0.892}{3\sqrt{3}} \int_{L_3}^{+\infty} \frac{dX_1}{(X_1)^{2/3}(X - X_1)} \tag{45c}$$

$$\Lambda_{10}(X) = \int_{L_1}^{0} \frac{P_{T,B}(X_1)dX_1}{X - X_1} \tag{46a}$$

$$\Lambda_{02}(X) = \int_{0}^{L_2} \frac{P(X_1)dX_1}{X - X_1} \tag{46b}$$

$$\Lambda_{23}(X) = \int_{L_2}^{L_3} \frac{P(X_1)dX_1}{X - X_1} \tag{46c}$$

The integrals in equations (45) are evaluated in closed form and those in equations (46) are evaluated by numerical quadrature.

The range of integrations of the integrals in equations (46) is segmented by using the mesh distribution $X(I)$ employed in the boundary-layer calculation, and the integrals in equations (46a) and (46c) are expressed as a finite sum of integrals over the mesh increments $X(I + 1) - X(I)$. The individual integrals over these increments are then evaluated in closed form by using a piecewise linear approximation for the pressure distribution $P_{T,B}(X)$ and/or $P(X)$ over the mesh increment. The integral in equation (46b) is evaluated with a piecewise linear approximation for the function $P(X) - \frac{3}{2} C_o^{2/3} X^{2/3}$, where C_o is the constant appearing in the Hakkinen-Rott similarity solution (eqs. (18)). With this procedure all integrations are second-order accurate. The displacement functions can be evaluated from a trapezoidal integration as follows:

$$A_{T,B}(I + 1) = A_{T,B}(I) + \left[X(I + 1) - X(I)\right] A'_{T,B}\left(I + \tfrac{1}{2}\right) \tag{47}$$

with $A'_{T,B}\left(I + \frac{1}{2}\right)$ evaluated from equations (44) to (46). Two constants of integration appear. These are evaluated from the asymptotic solutions given in equation (13b) at the initial station $X(1) = L_o$, which yields

$$A_{T,B}(I = 1) = 0.3265\left|L_o\right|^{-1} + \alpha C_{12}\left|L_o\right|^{1/6} \operatorname{sgn} Z - \alpha^2 C_{21}\left[\frac{1}{3}\ln\left|L_o\right| + \ln 3\left(2^{1/3}\right)\right]$$

$$+ \alpha^2\left(C_{21} + C_{22}\right) + \alpha^3 C_{33}\left|L_o\right|^{-1/6} \operatorname{sgn} Z \qquad (48)$$

This procedure results in a convenient method for determining the values of $A_{T,B}$ at the mesh points $X(I)$ given the pressure at the same points. A number of numerical experiments have been carried out for sequences of mesh distributions and for pressure distributions that could be integrated in closed form. These results clearly indicated that the quadrature errors reduced quadratically with mesh size and that the preceding evaluations of $A_{T,B}(X)$ were second-order accurate at all points of the mesh including those near the trailing edge. The results of this study will be presented in a separate publication.

Accuracy and Convergence Considerations

A number of numerical experiments were carried out to check the accuracy of the complete program. These tests were carried out for the symmetric problem (i.e., $\alpha = 0$) by using a version of the program that was modified to allow for the symmetry of the solution. The angle-of-attack terms were deleted and a symmetry condition was imposed on the wake axis. With the modified program it was necessary to compute the solution only in the upper half-plane; thus the number of mesh points required was reduced by one-half.

Calculations were performed to determine the effect of varying the locations of the upstream $(X = L_o)$ and downstream $(X = X_P)$ boundaries of the mesh and the position of the upper boundary y_M. The number of mesh points employed in the horizontal and vertical directions were also varied, as were the parameters controlling the relative spacing of the grid. Computations were carried out using up to 99 points normal to the plate and 300 points in the streamwise direction. These results indicated that a good distribution of mesh points is generated with the following choices.

For the y-mesh

$$y_M = 8.0 \qquad K_1 = 2/5 \qquad (49)$$

and 25 points are employed on the plate side $(J_P = 25)$ and 44 points on the wake side $(J_W = 44)$ of the trailing edge. Of the 44 points in the wake, 12 $(J_{inner} = 13)$ are dis-

tributed uniformly in the region $0 \leqq y \leqq 0.5555$. With these choices the minimum increment occurs on the axis and is equal to

$$(\Delta y)_{min} = 0.1333 \qquad (X < 0) \qquad (50a)$$

$$(\Delta y)_{min} = 0.0427 \qquad (X > 0) \qquad (50b)$$

The mesh spacing smoothly increases to a maximum at the upper boundary where it is equal to (for all X)

$$(\Delta y)_{max} = 0.8027 \qquad (51)$$

For the X-mesh the upstream L_o and downstream L_{max} boundaries are chosen as

$$L_o = -17 \qquad L_{max} = 30 \qquad (52)$$

Fifty-one points are employed on the plate and 124 points in the wake. The boundaries of the various segments in the wake are taken at

$$I_1 = 81 \qquad I_2 = 151 \qquad I_3 = 175 \qquad (53)$$

and, therefore, a total of 175 grid points are employed in the streamwise direction.

The initial station in the wake is taken at $I = 57$ which occurs at

$$X(57) = 0.004136 \qquad (54)$$

The minimum mesh increment on the plate occurs at the trailing edge and is equal to

$$(\Delta X)_{min} = 0.05 \qquad (X < 0) \qquad (55)$$

In the wake the minimum increment occurs at the wake initial station $X(57)$ and is equal to

$$(\Delta X)_{min} = 0.002432 \qquad (X > 0) \qquad (56)$$

These choices lead to very high concentrations of mesh points in the initial parts of the wake. About 10 points of the y-grid fall in the inner region of the wake initial profile where the solution is described by the Hakkinen-Rott similarity solution. Numerical

experiments have indicated that solutions on this mesh are accurate to about one part in the third decimal place.

Convergence criteria were set on both iterative loops employed in the program to achieve three-place accuracy. The error tolerance ϵ_1 used in the Newton-Raphson solution of the difference equation (see eq. (30)) was set at 10^{-2}. This resulted in solutions to the difference equations that are accurate to 10^{-8} or better in two cycles per streamwise step at most stations. A third cycle is occasionally required near the trailing edge.

The overall interaction between the boundary-layer and inviscid programs is continued until the solution has converged to the third decimal place. Twelve iterations were required to converge the main loop with $\omega = 0.15$ and $X_p \approx 3$. Each cycle consists of a sweep through the boundary layer and the evaluation of the Hilbert integral. Most of the computer time is taken in the boundary-layer routine. The computations were performed on an IBM 370/165 digital computer and required about 20 seconds per cycle, or about 4 minutes to complete the first 12 iterations. A total of 28 additional cycles were employed to move the terminal point X_p downstream to $X_p = 20.791$. The influence of the value of X_p on the upstream solution was investigated and was found to amount to an increment of no more than 0.002 in the solution at $X = X_p$, which decreased rapidly upstream. Similar conclusions hold for the angle-of-attack problem except that the computer times were about doubled because of additional mesh points on the lower side of the flow field.

The present program used significantly fewer iterations and less computer time than that required by similar methods developed by Jobe and Burggraf (ref. 6) to treat the zero angle-of-attack problem. This is apparently due to their use of a fixed point iteration scheme to solve the finite-difference equations and to the use of a separate iterative scheme to compute the pressure at each streamwise station. Jobe and Burggraf were able to use larger values of ω in the outer loop and, as a result, obtained solutions with somewhat fewer outer cycles. However, this advantage did not nearly overcome the longer cycle times required in their program. It should be pointed out, however, that the symmetric problem does not involve free parameters and, hence, needs to be solved just once. Therefore, computing efficiency is not a real issue in this problem. It was, however, important to develop an efficient code for the full problem since there are twice the number of mesh points and since solutions must be obtained for various values of the normalized incidence α.

RESULTS

The triple-deck formulation reduces the trailing-edge problem to one involving a single parameter α, a normalized angle of attack defined in equations (2). The computer

program described in the previous section has been employed to obtain solution for two values of α equal to 0 and 0.10. Initial estimates to start the iteration were obtained from the approximate solution of Messiter (ref. 2) for $\alpha = 0$ and the linear solution of Brown and Stewartson (ref. 3) for nonzero angles of attack. Numerical experiments carried out in the study indicates that the present solution for the symmetric case is accurate to three decimal places. The symmetric solution was obtained by using a special version of the code in which the angle-of-attack terms appearing in the boundary and initial conditions were set to zero. In addition, a symmetry condition was imposed on the axis (i.e., $\psi = \tau = 0$ at $y = 0$) and the solution was computed only in the upper half-plane. The solution for $\alpha = 0.10$ was obtained with an early version of the code that employed a somewhat coarser mesh and, hence, is likely accurate to just two decimal places.

The results obtained for the symmetric problem are compared with solutions of the triple-deck equations recently obtained by Jobe and Burggraf (ref. 6) and Veldman and Van De Vooren (ref. 7). The computations in these studies were based on finite-difference techniques that differed in a number of respects from the method employed here. The main difference being that a second-order Crank-Nicolson scheme was employed in references 6 and 7, while a Keller-Cebeci box scheme was employed in the present study. The computations in reference 6 were carried out on a nonuniform mesh using up to 180 points in the vertical direction and 480 points in the streamwise direction. In reference 7 a nonuniform mesh was employed with a maximum of 40 points in each direction. These are to be compared with the 24×175 point nonuniform mesh used in the present computation. The inviscid solution was obtained in reference 6 and in the present study from a numerical quadrature of the Hilbert integral. In reference 7 the inviscid solution was determined from a finite-difference solution of Laplace's equation in the outer deck by using a 40×40 point mesh distribution. The iterative techniques used in the present scheme appear to be more effective and require significantly less computer time than the methods employed in references 6 and 7. Comparisons given in this section indicate that the overall agreement between the three sets of solutions is quite good, with differences amounting to a few parts in third decimal places at most points of the flow field. However, the solutions of reference 6 are somewhat less accurate near the trailing edge due to the poor resolution of the trailing-edge singularity obtained with the uniform mesh distribution used in that study. The computation in reference 7 loses some accuracy in the far field due to the large mesh spacing used in that region.

Solutions to the symmetric problem are presented in figures 5 to 17. The pressure distribution on the axis is given in figures 5 to 7. The effect of the wake in generating a significant favorable pressure gradient on the plate is clearly shown in figure 5. The pressure starts from the free-stream level far upstream and falls to a value of

$$P_{TE} = -0.394 \tag{57}$$

at the trailing edge. This should be compared with the values of P_{TE} of -0.388 and -0.392 obtained in references 6 and 7, respectively. The pressure then rises steeply from this trailing-edge value to a small positive maximum and then approaches the free-stream value slowly from above. These results clearly show a large adverse pressure gradient in the wake just downstream of the trailing edge. The pressure gradient is bounded on the upstream side and is unbounded on the downstream side of the trailing edge. The numerical solution is seen to blend smoothly into the asymptotic far-field solution for $X \to \pm\infty$ and match smoothly with the singular solution at the trailing edge for $X \to 0^+$. The coefficient of the third term of the trailing-edge solution (eq. (17a)) has been extracted from the present numerical results as

$$P_1 = -0.52 \tag{58}$$

The agreement between the present solution and the solutions of references 6 and 7 is quite favorable, with the differences between the results being indiscernible on the scale of figure 5.

The pressure distribution near the trailing edge is shown on a greatly expanded scale in figure 6. Differences between the three sets of results are apparent on this scale. The present results and those of Veldman and Van De Vooren are virtually identical with the three term expansion given in equation (17a) with the constant P_1 given by equation (58). The use of a nonuniform mesh with a fine grid near the trailing edge provides excellent resolution of the singular trailing-edge behavior in the present calculations and in those of Veldman and Van De Vooren. The results of Jobe and Burggraf, which were obtained on a uniform mesh, definitely appear to have a higher truncation error and to lose some resolution as the origin on the wake side of the trailing edge is approached. Their results, however, appear to improve as the mesh size is reduced.

On the basis of analytical considerations, Stewartson in reference 1 has indicated that the pressure gradient is finite on the plate side of the trailing edge and that logarithmic terms must arise in the expansion of the pressure distribution as $X \to 0^-$. (See eq. (16a).) The present results plotted in figure 7 seem to confirm Stewartson's conjecture. In figure 7, the numerical solution for the pressure gradient is compared with the analytic expression given in equation (16a). The numerical constants P'_{TE}, P_2, and P_3 were extracted from the numerical solution and were found to have the following values:

$$P'_{TE} = -0.301 \qquad P_2 = 0.12 \qquad P_3 = -0.14 \tag{59}$$

This is to be compared with the value $P'_{TE} = -0.278$ given in reference 6. The numerical solution clearly indicates a vertical tangent at the origin and shows creditable agreement with the analytical solution using the constants given previously. Four mesh points in the region $X < -0.5$ fall on the analytical curve given in figure 7.

The solution for the skin friction is given in figure 8. The solution is seen to match smoothly to the weak interaction solution given in equation (13c). The results clearly show the strong effect of the wake-induced pressure gradient on the skin friction. The skin friction at the trailing edge is increased by a factor of λ_1 over the Blasius value, where

$$\lambda_1 = 1.351 \tag{60}$$

This is to be compared with the values of $\tau_w(0) = 1.343$ and $\tau_w(0) = 1.352$ predicted in references 6 and 7, respectively. Comparisons of the triple-deck solution with the second-order boundary-layer solution of Schneider and Denny (ref. 25) are given in reference 6.

The solution for the centerline velocity in the wake is given in figure 9, together with a comparison of the Goldstein solution for $X \to +\infty$ and with the Hakkinen-Rott solution for $X \to 0^-$. Both analytic solutions exhibit an $X^{1/3}$ behavior and appear as linear distributions in the scale used in the figure. Also included is a comparison with two terms of the Goldstein solution. The second term, involving the constant b_1, corresponds to a shift in the origin of the asymptotic solution. The value of the constant b_1 has been extracted from the present numerical solution, as will be discussed later in this section. It can be seen that the triple-deck solution provides a smooth blending between the trailing-edge and far-field solutions. The effect of the shift is clearly evident in the results.

In figure 10, the solution for the centerline velocity is compared with the results of references 6 and 7 on an expanded scale near the origin. The present results show good agreement with the solution of Veldman and Van De Vooren and with the singular solution of Hakkinen and Rott right to the trailing edge. The nonuniform mesh employed here and in reference 7 permits a very high resolution of the singular trailing-edge behavior. The results of Jobe and Burggraf (ref. 6) again show higher truncation errors and somewhat poorer resolution near the trailing edge owing to the larger mesh intervals employed in their uniform mesh solutions.

The solution of Veldman and Van De Vooren employs a highly stretched mesh with relatively large mesh increments in the region away from the trailing edge. The results in figure 10 indicate that this leads to somewhat larger truncation errors in the downstream region than those that arise in the present solution.

The present solution for the displacement function $A(X)$ is compared with the far-field asymptotic expansions in figure 11. Again the numerical solution blends smoothly

into the asymptotic solutions for $X \to \pm\infty$. The effect of the origin shift in the downstream solution is again evident in the comparison. The inclusions of the b_1 term in the asymptotic solution is seen to extend the region of agreement well into the near field. The results are seen to be in good agreement with the solutions given in references 6 and 7, with no apparent differences on the scale employed in figure 11.

Comparison of the present results for the slope of the displacement surface with the solutions of Jobe and Burggraf shows some discrepancy as indicated in figure 12. The dashed line in figure 12, representing the solution of reference 6, was obtained from a graphical reading of a figure in reference 6 using an automatic digitizer. Some of the differences are surely due to errors in reading the graphical data. However, the main differences are in the trailing-edge region, and these are likely caused by the larger grid spacing used in reference 6. The present results clearly show the vertical tangent at the origin implied by the singular solution given in equation (17b). This is seen more clearly on the expanded scale used in figure 13. In figure 13, the present numerical solution for $A'(X)$ is compared with the singular expansion given in equation (17b) and with the solution of reference 6 as tabulated in the thesis of Jobe (ref. 26). The present solution is seen to blend very smoothly with three terms of the singular solutions. The constants in equation (17b) were evaluated by fitting equation (17b) to the present numerical solutions and were found to have the following values:

$$A_{TE} = 0.338 \qquad A'_{TE} = 0.402 \qquad A_1^+ = -1.3 \qquad A_1^- = -2.1 \tag{61}$$

These are to be compared with the values $A_{TE} = 0.335$, $A'_{TE} = 0.335$, and $A_1^+ = 0.56$ given in reference 6. The results agree relatively well with the solution of reference 6 except for the grid point nearest the trailing edge and the values of the constant A_1^-.

The constant b_1 appearing in the second term of the far-field solution has been evaluated by fitting equations (14b) and (14c) to the present numerical solutions for $A(X)$ and $U(X,0)$. The results are denoted by $b_A(X)$ and $b_U(X)$ and are displayed as functions of X in figure 14. The results seem to approach a limiting value that is given by

$$b_1 = -0.285 \pm 0.005 \tag{62}$$

which is to be compared with the value $b_1 = -0.27 \pm 0.03$ quoted in reference 6. Also shown for comparison is a similar plot taken from reference 26. The difference between the two sets of results is likely caused by somewhat higher truncation error and by the abrupt termination procedure employed in the calculation of references 6 and 26.

The drag coefficient for the finite flat plate can be evaluated from an integration of the skin-friction distribution on the plate as follows:

$$C_D = 1.328R^{-1/2} + d_2R^{-7/8} + 0(R^{-1}) \tag{63a}$$

where the constant d_2 is given by

$$d_2 = 2\lambda^{-1/4} \int_{-\infty}^{\infty} [\tau(X,0) - 1]dX \tag{63b}$$

Use of the present solution for the skin friction and a trapezoidal integration of the preceding integral leads to the following evaluation:

$$d_2 = 2.660^{1} \tag{63c}$$

In figure 15 the drag coefficients predicted by equations (63) are compared with experimental data obtained in 1935 by Janour (ref. 8) for flow of oil over a finite flat plate. Also included is a comparison with solutions of the full Navier-Stokes equations recently obtained by Dennis in 1973 (as mentioned in the Introduction) for Reynolds numbers in the range $1 \leq R \leq 200$. The results in the figure show that the correction to the Blasius result is large in this range and that it is accurately predicted by equations (63) to within a few percent for Reynolds numbers as low as $R = 10$.

Dennis later extracted the value of d_2 by fitting an equation of the form of equation (63a) to his numerical solutions. His results for d_2 are plotted in figure 16 together with the limiting values (i.e., for $R \to +\infty$) predicted by the triple-deck solutions as obtained in the present study and in references 6 and 7. The agreement of all three triple-deck solutions with Dennis' results is quite good with the present solution yielding the best agreement.

The preceding results indicate that the triple-deck solution is accurate over a surprisingly wide range of Reynolds numbers. Indeed the maximum difference with the Dennis solution for the drag coefficient is about 8 percent at a Reynolds number R of 1. The close agreement with the Navier-Stokes solutions implies that the next term in the asymptotic solution, which is formally on the order of $0(R^{-1})$ must be very small. Further comparisons and discussions of the drag coefficient are given in references 6, 20, and 26.

Sato and Kuriki (ref. 9) carried out wind-tunnel experiments on the flow in the wake of a thin plate. The flow was determined to be two-dimensional. The plate was 300 millimeters long and the flow velocity was 10 meters/second. The investigators were primarily interested in exploring the transition of the wake from laminar to turbulent flow. They

[1] A value of $d_2 = 2.644$ attributed to the present authors in references 6 and 7 was obtained on a coarser mesh than the one employed in the present computations and is, consequently, less accurate than the above value.

measured mean as well as fluctuating velocity profiles in the wake. The Reynolds number of the test was 2.1×10^5 ($\epsilon = 0.216$). The mean velocity profile given in figure 17 was measured at a station 30 millimeters behind the trailing edge where the flow was fully laminar (the nonlinear transition region started about 40 to 60 millimeters behind the plate). At this Reynolds number the pressure peak predicted by the triple-deck theory occurs at 40 millimeters behind the plate. Thus, the measuring station for the profiles in figure 17 was in a region where the theory predicted a strong adverse pressure gradient.

The triple-deck solution was used to construct a composite velocity profile at $X = 30$ millimeters. The solution was represented as the sum of an "outer and inner solution" minus the "common part," as follows:

$$\frac{U_{comp}}{U_\infty} = f'(\eta) + 0.4945A(X)\left[f''(\eta) - f''(0)\right] + 0.1642\left(U_{inner} - Z\right) \tag{64a}$$

where

$$\eta = 0.4941Z \tag{64b}$$

and the physical distance normal to the wake axis is given by

$$y_{min} = 0.325Z \tag{64c}$$

The function $f(\eta)$ is the Blasius function for the semi-infinite flat plate solution and $U_{inner}(Z)$ is the triple-deck solution for the wake profile at $X = 2.49$. The displacement function at this station is given by

$$A(2.49) = 1.052 \tag{64d}$$

The profile given by equations (64) is compared with the measured profile of Sato and Kuriki in figure 17. The theoretical and experimental profiles are seen to be in good agreement across the entire wake. The main differences occur in the outer region where viscous and pressure gradient terms have been neglected in the theoretical solutions. Also indicated is the centerline velocity predicted by the one-term Goldstein solution. The effect of the interaction in reducing the centerline velocity is significant and readily discernible in this experiment. It is also of some interest to call attention to the fact that transition was observed to start at a station 40 millimeters behind the plate, which coincided with the location of the theoretical pressure peak in the wake. This result suggests that self-induced pressures may play an important role in the transition of a wake from laminar to turbulent flow. As a corollary it also indicates that the effect of wake-induced pressure gradients may have to be accounted for in theoretical transition calculations.

The numerical methods developed in the present investigation have been found to provide an effective means for solving the triple-deck equations. Because of the overall efficiency of the differencing and iterative techniques employed, it is practical to use these methods to solve the angle-of-attack problem. An early version of the code described in previous sections was used to obtain solutions for α (normalized angle of attack) equal to 0.10. This solution was obtained without the terms of $0(\alpha^2)$ or greater that appear in the outer boundary condition given in equations (26) to (27) and in the initial condition given by equations (12). These terms are quite small and are believed to have a small influence on the solution at the value $\alpha = 0.10$ for which the computations are carried out.[2]

In figure 18 the solution for the pressure distributions on the top and bottom of the plate and on the wake axis is compared with an approximate solution developed in reference 3. The approximate solution was based on a simple linearization of the triple equations about a linear streamwise velocity profile. As was noted in reference 3, the linearization is clearly not valid in the wake, where the velocity gradient $\partial U/\partial y$ must vanish on the axis. However, the errors in the wake are not expected to have a strong influence on the solution upstream of the trailing edge. If this holds true, the linearized solution should provide a reasonably good approximation to the angle-of-attack solution. The results in figure 18 bear this out. The agreement between the present numerical solution of the full triple-deck equations and the linearized solution given in reference 3 is seen to be quite good. The effect of incidence on the pressure distribution in the wake is barely noticeable on the scale used in figure 18. The circulation constant a_1 appearing in the formula for the viscous correction to the lift coefficient in equations (4) and (5) is determined as part of the present solution and is given as

$$a_1 = 0.55 \tag{65}$$

This is to be compared with the value determined from the linearized solution of Brown and Stewartson, namely

$$a_1 = 0.79 \tag{66}$$

The agreement for a_1 is not nearly as good as for the pressure distribution but is probably as good as one should expect from such a simple approximation.

In figure 19, the numerical solution for the pressure distribution is compared with the inviscid solution on the plate and with asymptotic solution valid for upstream. The numerical solution is seen to blend smoothly into the upstream asymptotic solution. Comparison with the zero angle-of-attack solution given in figure 5 indicates that the approach to the far-field solution is much slower in the angle-of-attack case. The difference

---

[2]Computations including all terms appearing in equations (26) to (29) have been carried out since this paper was written and the results confirm this conclusion.

between the numerical and inviscid solutions in the far field is due mainly to the circulation term a_1. This term can be interpreted as a shift of the origin in the far-field asymptotic solution for $X \to -\infty$. The effect of the shift is clearly evident in the comparison in figure 19. The results in figure 19 clearly show the large changes in the inviscid pressure distribution induced by the wake. These changes take two main forms: one is the shift in the pressure distribution in the far field mentioned previously, and the other is the complete change in the shape of the pressure distribution near the trailing edge.

The effect of the induced pressures on the solution for the skin friction is indicated in figure 20. In this figure, the numerical solution for the skin friction on the top and bottom of the plate is compared with the asymptotic solution valid far upstream. The numerical solution is seen to join smoothly to the asymptotic solution. The far-field solution plotted in figure 20 contains three terms: the basic Blasius value, the second due to inviscid pressure gradients induced by incidence, and the third term due to the favorable pressure gradient induced by the wake interaction. These terms combine to yield a skin-friction variation that is quite small except very close to the trailing edge. The effect of incidence is seen to have a fairly large effect on the value of skin friction at the trailing edge, which was equal to $C_f(0) = 1.349$ for $\alpha = 0$. Clearly, a much larger value of incidence will be required to drive the skin friction to zero on the upper service. The present result seems to indicate that the point of vanishing skin friction should first arise at a station upstream of the trailing edge.

The solution for the displacement functions $A_T(X)$ and $A_B(X)$ is given in figure 21 where it is compared with the far-field asymptotic solutions. The strong effect of incidence in displacing the wake centerline is clearly evident in this result. Again, attention is called to the smooth blending of the numerical and asymptotic solutions in the far field.

TURBULENT TRAILING-EDGE FLOWS

The numerical solutions obtained in this study and in references 6 and 7 have completely confirmed the triple-deck model and the local asymptotic solutions developed in references 1 to 3. These works provide a sound theoretical framework for analyzing laminar interactions at trailing edges of streamlined bodies. Unfortunately, the boundary layer on an airfoil usually undergoes transition to turbulent flow at the Reynolds numbers of interest. Most theoretical methods for predicting the effect of boundary layers on airfoil characteristics are based on classical second-order boundary-layer theory. Although not generally recognized, second-order boundary-layer theory for turbulent flows breaks down at airfoil trailing edges. Consequently, the theory does not provide a satisfactory basis for computing boundary-layer corrections to inviscid airfoil solutions. It is, therefore, important to develop a systematic theory for treating turbulent interactions in airfoil problems.

In the present study, a formal asymptotic theory has been developed for turbulent interacting flows, following broadly along the lines of the laminar triple-deck theories. Of course, turbulent boundary layers differ greatly from laminar flows and are controlled by quite dissimilar physical mechanisms. Particularly significant is the fact that turbulent boundary layers tend to retain high velocities much closer to the wall than in a laminar flow. This effect is one of the main reasons for the small upstream influence observed in turbulent interactions. However, the general idea of the triple-deck approach in seeking formal asymptotic solutions of the Navier-Stokes equations in the limit of large Reynolds numbers is also useful for the turbulent problem.

Accordingly, solutions of the turbulent airfoil problem will be developed as formal asymptotic expansions of the full Navier-Stokes equations in the limit $R \to \infty$. The turbulent analysis is carried out by using the basic framework developed in references 1 to 3 for laminar trailing-edge problems. Incompressible flow over a thin airfoil with a cusped or nearly cusped trailing edge at angle of attack is considered. The airfoil is assumed sufficiently thin so that the inviscid flow is described to lowest order by the flat plate solution given, for example, by equations (3) and (4) of this paper. Here, however, the angle of attack α^* is assumed to be 0(1) and not necessarily small. Transition is assumed to occur upstream of the trailing edge and the boundary layers are assumed to be fully developed turbulent flows in the trailing-edge region. More specifically, the velocity profiles in the noninteracting region are assumed to have a small defect form in the main part of the boundary layer and the usual logarithmic behavior near the wall.

In this section, the main features of a turbulent interaction theory that can be developed under these general conditions are outlined. First the behavior of boundary-layer theory near trailing edges is examined. It is shown that a singularity arises in the solution which causes a breakdown of the second-order theory near trailing edges. This analysis will show that a Kutta condition for the second-order solution cannot be satisfied and that the lift correction cannot be determined.

The failure of second-order theory is resolved by the introduction of a local solution that correctly describes the flow near trailing edges. The local solution is shown to have a three-layer structure that superficially resembles the triple-deck structure of the laminar problem. However, in the turbulent problem the physical mechanisms leading to this structure and the basic equations holding in each region are very different from those arising in the laminar flows.

In the present discussion, only a very brief description of the turbulent interaction theory is presented. The asymptotic structure of the local solutions governing the flow near the trailing edge will be described and the boundary-value problem that must be solved to complete the solution in the trailing-edge region will be outlined. Also a simple solution for the skin friction in the trailing-edge region that follows from the theory is

presented. The skin-friction solution is compared with experimental data of Schubauer and Klebanoff (ref. 18) and with numerical solutions of the boundary-layer equations.

Second-Order Solution

The second-order solution for viscous flow over an airfoil is determined in the following steps:

(1) Determine the inviscid solution for flow over the prescribed airfoil shape and compute the pressure distribution on the surface

(2) Solve the boundary-layer equations with the pressure distribution obtained from the inviscid solution and compute the displacement thickness

(3) Use the displacement surface to compute the equivalent source/sink distribution on the airfoil and wake surface and solve the inviscid equations with the source distribution as a surface boundary condition. Alternatively, the displacement thickness can be used to form an equivalent airfoil shape that serves as a new geometry in the inviscid solution.

This well-known procedure can be embedded in a formal asymptotic expansion for large Reynolds numbers. However, because of the presence of a singularity in the inviscid solution, this expansion is not uniformly valid at trailing edges. Consequently, the second-order solution cannot be completed and the boundary-layer corrections to the lift coefficient cannot be determined. Previous airfoil calculations based on second-order boundary-layer concepts relied on numerical smearing of the trailing-edge singularity to obtain solutions.

A singularity appears at the trailing edge in the inviscid solution for all lifting airfoils with a sharp trailing edge. For an airfoil with a cusped trailing edge, the pressure distribution on the surface exhibits a square-root behavior. This is illustrated in figure 22 where the steps leading to the nonuniformity of the second-order theory are outlined. Near the trailing edge, the pressure distribution is given by

$$P^* = P^*_{TE} - \rho U^{*2}_{TE}\left(C_\alpha \sqrt{-x^*/L}\ \operatorname{sgn} y + \ldots\right) \tag{67a}$$

where L is the airfoil chord and C_α is a constant that depends on the incidence α^* and the shape of airfoil. For a flat plate (or a sufficiently thin airfoil) C_α can be determined from the solution given in equations (3), namely

$$C_\alpha = \alpha^* \tag{67b}$$

and $P^*_{TE} = p_\infty$ and $U^*_{TE} = U_\infty$.

The behavior of the displacement thickness near the trailing edge can be determined from the momentum integral equation

$$d\delta_2^* + \delta_2^* dx^* (H + 2) \frac{dU_e^*}{U_e^* dx^*} = \frac{1}{2} C_f \tag{68}$$

where δ_2^* is the momentum thickness, H is the shape factor, U_e^* is the streamwise velocity external to the boundary layer, and C_f is the skin-friction coefficient. The displacement thickness δ_1^* is given by

$$\delta_1^* = H\delta_2^* \tag{69}$$

With the external velocity evaluated from the inviscid solution (eqs. (67)), the second term in equation (68) is unbounded at the trailing edge. Since the variation of skin friction due to pressure variations can be shown to be equal to the order of the pressure change, the singular acceleration term in equation (68) can only be balanced by the gradient of momentum thickness. Thus, equations (67) to (69) lead to the following expansion for the displacement thickness as $x^* \to 0$:

$$\delta_{1,T}^* = \delta_{1,T}^*(0)\left\{1 - C_\alpha\left[H_T(0) + 2\right]\sqrt{-x^*/L} + \ldots\right\} \qquad (x^* < 0) \tag{70a}$$

$$\delta_{1,B}^* = \delta_{1,B}^*(0)\left\{1 + C_\alpha\left[H_B(0) + 2\right]\sqrt{-x^*/L} + \ldots\right\} \qquad (x^* < 0) \tag{70b}$$

where the subscripts T and B refer to the top and bottom of the airfoil, respectively. The boundary layer thickens on the top and thins on the bottom of the airfoil due to the imposed pressure distribution. This leads to an equivalent camber distribution δ_c^* given by

$$\delta_c^* = \frac{1}{2}\left(\delta_{1,T}^* - \delta_{1,B}^*\right) = \delta_c^*(0) + B_\alpha\sqrt{-x^*/L} + \ldots \tag{71a}$$

where

$$\delta_c^*(0) = \frac{1}{2}\left[\delta_{1,T}^*(0) - \delta_{1,B}^*(0)\right] \tag{71b}$$

$$B_\alpha = -\frac{1}{2} C_\alpha \left[\delta_{1,T}^*\left(H_T + 2\right) - \delta_{1,B}^*\left(H_B + 2\right)\right]_{x^*=0} \tag{71c}$$

The slope of the equivalent camber distribution given in equations (71) is singular at the trailing edge. The antisymmetric part of the second-order outer solution is determined by computing the inviscid flow over this camber distribution. It follows from potential

flow considerations that the second-order solution for the surface velocity must have the following behavior for $x^* \to 0^-$:

$$\frac{U^*}{U^*_{TE}} = 1 + \left[C_\alpha \sqrt{-x^*/L} + \frac{(B_\alpha/\pi) \ln (x^*/L) + \Delta\Gamma}{\sqrt{-x^*/L}} + \ldots \right] \operatorname{sgn} y \tag{72}$$

where C_α and B_α are the constants defined previously and $\Delta\Gamma$ is an arbitrary constant.

The first two terms in equation (72) arise from the inviscid solution and the last two are induced by the interaction. Notice that both interaction terms are singular. The logarithmic term is induced by the singularity in the camber distribution, while the $\Delta\Gamma$ term is an arbitrary homogeneous solution that satisfies Laplace's equations and the boundary conditions. Ordinarily this term would be excluded by the Kutta condition, which requires the solution to be bounded at the trailing edge. It is clear from equation (72) that this condition cannot be satisfied for any value of the constant $\Delta\Gamma$. Thus, the second-order solution cannot be completed and the boundary-layer correction to lift cannot be determined. It is curious that this conclusion, which follows from the simple analysis given previously in this paper, has gone unrecognized in previous viscous airfoil analyses.

Interaction Theory

The results given previously clearly demonstrate that the standard second-order boundary-layer theory is not uniformly valid at trailing edges. To develop complete solutions of viscous airfoil problems, the basic theory must be corrected to better account for the flow near the trailing edge. In the present investigations, the method of matched asymptotic expansions was used to develop formal solutions for the trailing-edge region. This approach is based on the time-averaged Navier-Stokes equations with a turbulence closure employing a turbulent kinetic equation and an algebraic length-scale relation. Solutions were developed in terms of a small parameter ϵ which here is related to the friction velocity u^*_τ in the noninteracting region upstream of the trailing edge. That is,

$$\epsilon = \frac{u^*_{\tau,o}}{U^*_\infty} = \sqrt{\frac{1}{2} C_{f,o}} \tag{73}$$

where $C_{f,o}$ is the skin-friction coefficient at the trailing edge, as determined from solution of the noninteracting boundary-layer equations on the top of the airfoil. Asymptotic solutions are developed for $R \to \infty$ or equivalently for $\epsilon \to 0$. The analysis follows very closely a similar theory developed for interactions between turbulent boundary layers and normal shock waves in reference 16.

In the brief discussion of the theory given here, only a general description of the main results of the analysis will be provided. In addition, the present discussion will be limited to incompressible flows. A more complete discussion of the analysis leading to these results along with a simple extension to compressible trailing-edge flows will be provided in future publications.

From the present analysis, it has been determined that the streamwise extent of the interaction region at the trailing edge is on the order of a boundary-layer thickness; that is, $\Delta y^* \approx \delta^* \approx \epsilon L$. The flow near the trailing edge was found to develop a multilayered structure, as illustrated in figure 23. The solution upstream of the interaction is divided into standard potential flow and boundary-layer regions over a streamwise length scale $0(L)$. The solution in the boundary layer has a two-layer structure typical of turbulent flows; an outer wake-like region and an inner wall layer. The velocity profile in the outer region has a small defect form, which on the top of the plate can be written in the form

$$\frac{U^*}{U^*_{e,T}} = 1 + \epsilon f\left(y^*/\delta^*_T, x^*\right) \tag{74}$$

where U^*_e is the velocity at the edge of the boundary layer and δ^*_T is the local boundary-layer thickness. The velocity profile in the inner layer is expressed in a law of the wall form

$$\frac{U^*}{U^*_{e,T}} = \epsilon F(y^+, x^*) \tag{75a}$$

where y^+ is a wall variable defined by

$$y^+ = y^* u^*_{\tau,T}/\nu \tag{75b}$$

where ν is the kinematic coefficient of viscosity. Similar expressions hold for the boundary-layer profiles on the lower surface. The solution for noninteracting turbulent boundary layers has been embedded in a formal asymptotic structure by Mellor (ref. 12), Yajnik (ref. 13), and Bush and Fendell (refs. 14 and 15). These authors have shown that the law of the wall and velocity defect profiles appear as the leading terms of an asymptotic expansion for $R \to \infty$. Thus, fully developed turbulent boundary-layer flows can be viewed as limiting solutions valid in this limit. The present analysis should be considered as an extension of these works to the trailing-edge interaction problem.

The solution in the interaction region develops the three-layer structure illustrated in figure 23.

The three layers required in the solution are

(1) An outer, basically inviscid rotational stream. This region includes most of the boundary layer and a part of the irrotational flow outside the boundary layer that is on the order of a boundary-layer thickness.

(2) An inner wall layer that is a continuation of the wall layer from upstream.

(3) An intermediate, or blending layer that occurs between the outer and wall layers. The blending layer is thinner than the outer layer but thicker than the wall layer.

The wall-layer thickness is defined in terms of the parameter $\hat{\epsilon}$ introduced by Mellor in reference 12

$$\Delta y^* \approx \epsilon\hat{\epsilon}L \tag{76a}$$

where

$$\hat{\epsilon} = \left[\epsilon^2 R\right]^{-1} \tag{76b}$$

In the outer layer both the Reynolds and viscous stresses are small compared to the inertia terms in the momentum equation. Vorticity is generated in the upstream boundary layers and is convected, unchanged, along streamlines in the trailing-edge region. This leads to a description of the flow as an inviscid rotational stream. A similar model was first proposed by Lighthill in 1953 (ref. 28) for treating interactions of oblique shock waves with turbulent boundary layers at supersonic speeds.

The flow in the inner layer is a local equilibrium flow in the sense of Townsend (ref. 29). To lowest order, the total stress (viscous plus Reynolds stresses) is constant across the layer and the solution is completely determined by the local skin friction.

An intermediate region is required because of a mismatch that develops between the Reynolds stresses in the inner and outer layers. In the outer layer, the Reynolds stresses are frozen at their upstream values. In the inner layer, the Reynolds stresses are in a local equilibrium determined by the wall friction because of the small-scale structure of the turbulence in this region. As a result, a discontinuity in Reynolds stresses develops between the inner and outer regions. This discontinuity is resolved by the blending layer. Solutions in the blending layer are governed by linearized boundary-layer equations that involve Reynolds stresses, but not viscous stresses. Turbulent closure models are required to complete the lowest order solutions in the wall and blending layer regions but not in the outer region. Displacement effects generated by the two inner layers are small and do not affect the first few terms of the solution in the inviscid outer region. Thus, the leading terms of the outer solution can be determined without consideration of the flow near the wall.

Next the form of the expansions in each region is considered. The expansion parameter ϵ defined in equation (73) is equal to the friction velocity of the upstream flow on the top of the airfoil. It should not be confused with the previous definition of ϵ used in the laminar study $\left(\text{i.e., } \epsilon_{\text{laminar}} = R^{-1/8}\right)$.

Outer Layer

The coordinate stretchings for the outer region are given by

$$X = (x^*/L)\epsilon^{-1} \qquad y = (y^*/L)\epsilon^{-1} \tag{77}$$

where the coordinate system employed in the laminar study is used. There will be some minor differences from the notation used for the laminar analysis but the changes will be clear and should not cause confusion.

The solution in the outer layer is dominated by contributions from the irrotational airfoil solution. The first terms in the expansion are obtained by expressing the airfoil solution in the inner variables defined in equations (77) and expanding the result in powers of ϵ. The next term comes from the upstream boundary layer and is determined by simply adding the defect part of the upstream profile to the irrotational contribution.

Physically, this approximation is based on the idea that velocity variation across the boundary layer is small in the limit of large Reynolds numbers. (See eq. (74).) Thus, the physical picture is one of a basically irrotational flow that is slightly perturbed by small shear flow disturbances near the wall. The resulting linear superposition of the boundary-layer and inviscid solutions leaves the pressure distribution in the field and the lift coefficient of the airfoil unchanged. The nonlinear interaction of these terms produces perturbations in the pressure distribution and lift coefficient. Thus, the expansion in the outer region is written in the form

$$\frac{\psi^*}{U^*_{TE}} \equiv \psi = y + \epsilon^{1/2}\psi_{inv}(X,y) + \epsilon\psi_{BL}(y) + \epsilon^{3/2}\psi'(X,y) + \ldots \tag{78a}$$

$$\frac{u^*}{U^*_{TE}} \equiv u = 1 + \epsilon^{1/2}u_{inv}(X,y) + \epsilon u_{BL}(y) + \epsilon^{3/2}u'(X,y) + \ldots \tag{78b}$$

where ψ and u are the nondimensional stream function and the streamwise velocity component, respectively, U^*_{TE} is the velocity at the trailing edge predicted by the irrotational outer solution, and $*$ denotes the corresponding dimensional quantities. The velocity components u and v are related to the stream function by the usual relations

$$u = \partial\psi/\partial y \qquad v = -\partial\psi/\partial X \tag{79}$$

The first two terms in equations (78) arise from the airfoil solution written in inner variables and then expanded in powers of ϵ. For a general airfoil with a cusped trailing edge this yields the result

$$\psi_{inv} = -\frac{2}{3} C_\alpha r^{3/2} \cos\frac{3}{2}\theta \tag{80a}$$

$$u_{inv} = C_\alpha r^{1/2} \sin\frac{1}{2}\theta \tag{80b}$$

where r and θ are polar coordinates, with θ measured from the positive X-axis, given by

$$r = \sqrt{x^2 + y^2} \tag{81a}$$

$$\theta = \tan^{-1}(y/X) \tag{81b}$$

Substitution of the assumed expansion into the time-averaged Navier-Stokes equations leads to the following equation for the perturbation stream function:

$$\nabla^2\psi' = -\zeta'(X,y) = -\frac{d^2u_{BL}(y)}{dy^2}\,\psi_{inv}(X,y) \tag{82}$$

where ∇^2 is the Laplacian operator and ζ' is the perturbation vorticity. This is a simple Poisson equation that relates the disturbance stream function to the perturbation in vorticity ζ'. The vorticity perturbation arises from the convection of the vorticity in the upstream boundary layer along the curved streamline of the irrotational airfoil solution, as illustrated in figure 24.

The Poisson equation must be solved subject to the boundary conditions

$$\psi'(X,y) \to 0 \qquad (r \to \infty) \tag{83a}$$

$$v' = -\frac{\partial\psi'}{\partial x} = 0 \qquad (y = 0;\ x \leq 0) \tag{83b}$$

where v' is the perturbation velocity normal to the surface. The perturbations in streamwise velocity and static pressure are given by the relations

$$u' = \frac{\partial\psi'}{\partial y} \tag{84a}$$

$$p' = -u' = -\frac{\partial\psi'}{\partial y} \tag{84b}$$

These boundary conditions lead to well-posed boundary-value problems for the outer solution. The outer solution leads to a "slip" velocity on the surface that is resolved by the inner layers.

The solution of the boundary-value problem can be represented as the sum of a particular solution plus a complementary solution. The particular solution satisfies equation (82) but not the boundary conditions. This solution leads to a downwash on the surface that violates the boundary condition on v' (eq. (83a)). The complementary solution is a solution of Laplace's equation that cancels this downwash. The solution for the particular integral depends on the form of the initial velocity profile $u_{BL}(y)$ and on the expression for the irrotational stream function ψ_{inv}. For general profiles, the particular and homogeneous solutions must be found by numerical means. However, if the initial profile is represented by a Coles law of the wall/law of the wake correlation, a closed-form expression for the particular integral can be found by analytic function theory. Coles form for the defect profile on the upper surface can be written in the form

$$u_{BL}(y) = \begin{cases} \frac{1}{\kappa}\ln\left(y/\delta_T\right) - \frac{\tilde{\pi}_T}{\kappa} W\left(y/\delta_T\right) & \left(0 \leq y \leq \delta_T\right) \\ 0 & \left(\delta_T < y\right) \end{cases} \tag{85}$$

where δ_T is a nondimensional boundary-layer thickness defined by the relation

$$\delta_T^* \equiv \epsilon L \delta_T \tag{86}$$

κ is the Karman constant, $\tilde{\pi}_T$ is the Coles wake parameter, and $W\left(y/\delta_T\right)$ is the wake function which can be represented by a simple polynomial approximation to the cosine function usually employed in this description. Similar expressions hold for the profile on the lower surface.

The particular integral evaluated in this fashion leads to closed-form expressions for the downwash velocity on the top and bottom of the plate. The homogeneous solution which cancels this downwash can be found in the usual way from thin airfoil theory. This leads to a representation of the homogeneous solution in terms of a Hilbert integral that must, in general, be evaluated by numerical quadrature. A Kutta condition, requiring the solution to be finite at the trailing edge, is imposed as part of the solution of the homogeneous problem. This condition determines the value of an arbitrary constant appearing in the trailing-edge solution that is directly related to the circulation constant $\Delta\Gamma$ appearing in the second-order boundary-layer solution (eq. (72)). Matching the trailing-edge solution to the second-order solution valid outside the trailing-edge region leads to an expression for the lift coefficient in the form

$$C_L = 2\pi\alpha^*\left(1 + a_1\epsilon^2 \ln \epsilon + a_2\epsilon^2 + \ldots\right) \tag{87}$$

where a_1 is a known constant and a_2 is a constant to be determined from a complete solution of the trailing-edge problem. The constant a_1 as determined by matching to the upstream solution (eq. (72)) is given by

$$a_1 = 1/\pi\left[\delta_{1,T}\left(H_T + 2\right) - \delta_{1,B}\left(H_B + 2\right)\right]_{X=0} \tag{88}$$

where $\delta_{1T,B}$ and $H_{T,B}$ are the (nondimensional) displacement thicknesses and shape factors at the trailing edge, respectively, as determined from the noninteraction boundary-layer solution. The nondimensional displacement thicknesses $\delta_{1T,B}$ are defined by the relation

$$\delta^*_{1T,B} = \epsilon^2 L \delta_{1T,B} \tag{89}$$

where $\delta^*_{1T,B}$ are the dimensional displacement thicknesses. Notice that the leading correction to the lift coefficient, as given in equation (87) is $0\left(\epsilon^2 \ln \epsilon\right)$. This term is completely missed in standard second-order theory which leads to a correction that is $0\left(\epsilon^2\right)$.

Equations (87) and (88) indicate that the lift correction is due primarily to the difference in boundary-layer thicknesses on the top and bottom of the airfoil. In the usual situation, $\delta_{1,T} > \delta_{1,B}$, and the effect of the log term is to reduce the lift coefficient. The effect of this term is most important on rear-loaded airfoils where the rear loading tends to dramatically increase the difference in boundary-layer thickness on the top and bottom of an airfoil. The effect of the shape of the boundary-layer profiles also influences the lift correction through the values of H_T and H_B appearing in equation (88). Rear loading tends to make the boundary layers less full on the top of the airfoil compared with the bottom. This implies that $H_T > H_B$ and this, in turn, also leads to a reduction in lift. This effect is formally of higher order since

$$H_{T,B} = 1 + 0(\epsilon) \qquad (R \to \infty) \tag{90}$$

However, in practice, H is significantly different from one at Reynolds number of interest (e.g., $H \approx 1.4$ for a flat plate at $R \approx 10^6$) and this effect can be numerically significant.

Inner Layers

Next briefly the form of the expansions in the two inner layers near the wall is considered. (See fig. 23.) Only the solution on the airfoil surface upstream of the trailing

edge is considered. The evolution of the inner layers into the wake leads to a similar structure. However, solutions in the inner layers of the wake are much more complex and have not yet been fully developed. A major uncertainty in the wake solution is concerned with the choice of a closure hypothesis to properly deal with a change in the sign of the Reynolds stress near the axis.

Only the solutions on the upper surface are dealt with explicitly. The expressions to be presented also hold on the lower side with an obvious change of notation. In the innermost layer the solutions for the streamwise velocity u^* and Reynolds stress τ^* are represented in the form of a law of the wall as

$$u^* = u^+ \sqrt{\tau_w^*(X;\epsilon)/\rho}\,(y^+, X;\epsilon) \tag{91a}$$

$$\tau^* = \tau_w^*(X;\epsilon)\tau^+(y^+, X;\epsilon) \tag{91b}$$

$$y^* = y^+ \nu \Big/ \sqrt{\tau_w^*/\rho} \tag{91c}$$

where $\tau_w^*(X;\epsilon)$ is the skin friction and u^+, τ^+, and y^+ are nondimensional wall-layer variables.

Substitution of these variables into the time-averaged Navier-Stokes equations with $\epsilon \to 0$ leads to the well-known condition that the total stress (laminar plus Reynolds stresses) is constant across the wall layer to all orders in ϵ. This conclusion follows from the fact that the wall-layer thickness is transcendentally small in ϵ. The wall-layer formulation is completed by the choice of a closure condition relating Reynolds stress to mean velocity. Analysis indicates that a balance of production and dissipation in the wall layer is a rational result that follows from the turbulent energy equation in the limit $\epsilon \to 0$. With the usual model of dissipation this leads to a mixing length formula

$$\tau^+ = \ell^2(y^+)(\partial u^+/\partial y^+)^2 \tag{92}$$

where $\ell(y^+)$ is the mixing length distribution. In this formulation the choice of $\ell(y^+)$ is strictly empirical. Careful consideration of the magnitude of the pressure gradients in the present problem indicates that the choices commonly used for moderate-pressure-gradient flows are appropriate here. For example, the two-layer model of Cebeci and Smith with a Van Driest damping factor is known to give very accurate solutions in incompressible wall layers. It is known that the mixing length distribution is linear for large y^+ and that this leads to the usual logarithmic velocity profile for $y^+ \to \infty$. Thus, if

$$\ell(y^+) = \kappa y^+ \qquad (y^+ \to \infty) \tag{93}$$

where κ is the Karman constant, it follows that

$$u^* \to \sqrt{\tau_w^*(X;\epsilon)/\rho}\left(\kappa^{-1} \ln y^+ + B^+\right) \qquad (y^+ \to \infty) \qquad (94a)$$

$$\tau^* \to \tau_w^*(X;\epsilon) \qquad (y^+ \to \infty) \qquad (94b)$$

where B^+ is a universal constant, independent of the local value of skin friction. With $\tau^*(X;\epsilon)$ expanded in a series in ϵ, the preceding result leads to an asymptotic solution for $\epsilon \to 0$ and $y^+ \to \infty$ that must be matched to the inner limit of the outer solution.

The solution for the velocity in the outer inviscid region has a similar behavior for $y \to 0$. However, because the Reynolds stresses are frozen in the outer region, the coefficient of the logarithmic term in the outer solution remains constant, equal to the friction velocity in the noninteracting boundary layer upstream. Thus the solution in the wall layer does not match the outer solution. It follows that an intermediate or blending layer must be inserted between the outer and wall layers in order to obtain a continuous solution for the Reynolds stresses across the boundary layer.

The requirement that the Reynolds stress be continuous leads to the condition that the shear stress term must be retained as a leading term in the streamwise momentum equation in the limit $\epsilon \to 0$. This condition determines the thickness of the blending layer to be $0(\epsilon^2 L)$. Thus a new stretched variable $\hat{y}$ is introduced to represent the solution in the blending layer, where

$$y^* = \epsilon^2 L \hat{y} \qquad (95)$$

Consideration of the form of the velocity profile in the upstream region and in the outer and wall layers leads to an assumption for a solution in the blending layer of the form

$$u = 1 + \epsilon^{1/2} u_{inv}(X,0) + \epsilon \ln \epsilon (1/\kappa) + \epsilon \hat{u}_{BL}(\hat{y}) + \epsilon^{3/2} \ln \epsilon \hat{u}_{21}(X) + \epsilon^{3/2} \hat{u}_{22}(X,y) + \ldots \qquad (96a)$$

$$v = \epsilon^{3/2} \hat{v}_2(X,\hat{y}) + \ldots \qquad (96b)$$

$$P = P_{TE} + \epsilon^{1/2} P_{inv}(X) + \epsilon^{3/2} \hat{P}_2(X) + \ldots \qquad (96c)$$

$$\tau = \epsilon^2 \left[1 + \epsilon^{1/2} \hat{\tau}_2(X,\hat{y}) + \epsilon^{3/2} \ln \epsilon \hat{\tau}_{31}(X) + \epsilon^{3/2} \hat{\tau}_{32}(X,\hat{y}) + \ldots\right] \qquad (96d)$$

where $u_{inv}(X,0)$ and $\hat{u}_{BL}(\hat{y})$ are deduced from equations (80b) and (85) and are given by

$$u_{inv}(X,0) = C_\alpha \sqrt{-X}\ \mathrm{sgn}\ y \tag{97a}$$

$$\hat{u}_{BL}(\hat{y}) = \kappa^{-1}\left[\ln\left(\hat{y}/\delta_T\right) - 2\tilde{\pi}_T\right] \tag{97b}$$

The ln terms appearing in the preceding expansions are required in order to match similar logarithmic terms in the inner expansions of the outer solution. These terms enter the expansion from the logarithmic behavior of the initial profile for small y. Consideration of the transverse momentum equation leads to the conclusion that the pressure is constant across the blending layer to the order considered in equation (96c). Thus the unknown function $\hat{P}_2(X)$ appearing in equation (96c) can be identified with the surface value of the pressure distribution of the outer solution. The requirement that the blending layer solution match the solution in the wall layer leads to the conclusion that the expansion for the Reynolds stress must have the same form as the expansion for the streamwise velocity component. It also follows that the relative change in skin friction in the trailing-edge region is on the order of the pressure change; that is, $\Delta_\tau/\epsilon^2 = 0(\epsilon^{1/2})$ as indicated in equation (96d).

Substitution of the preceding expansions into the momentum equation leads to the simple result

$$\hat{u}_{21}(X) = -\kappa^{-1} u_{inv}(X,0) \tag{98}$$

The solution for the vertical velocity component $\hat{v}_2$ is obtained from integration of the continuity equation

$$\hat{v}_2(X,\hat{y}) = -\left[du_{inv}(X,0)/dX\right]\hat{y} \tag{99}$$

The solutions for $\hat{u}_{22}$ and $\hat{\tau}_2$ are governed by two coupled first-order, linear, partial differential equations. These equations are derived from the streamwise momentum equation and from a turbulent closure hypothesis relating Reynolds stress to mean velocity. Since the pressure gradients on an airfoil can be relatively large, the closure assumption is based on the turbulent energy equation. Since the solution of these equations is not being considered in this presentation, they will not be written out here. Note simply that the momentum equation leads to a balance of linearized convective terms with shear stress and pressure gradient terms. Only the Reynolds stresses contribute to the shear stress gradients. The pressure gradient term is impressed from the outer inviscid solution $\left(dP_2(X)/dX\right)$.

The turbulent energy equation leads to a balance of advection, production, and dissipation of the Reynolds stress perturbation $\hat{\tau}_2$. The contribution from pressure diffusion and other terms in the energy equation are formally smaller than these main terms.

The present formulation leads to a simple form for the skin friction that is independent of the particular closure model assumed in the analysis. Matching of the blending and wall-layer solutions for u^* given in equations (94) and (96) leads to the following expression for the skin-friction coefficient:

$$\frac{C_f(X)}{C_{f,o}} = 1 - C_p(X;\epsilon) + 2\left(\frac{\epsilon}{\kappa} \ln \frac{\epsilon}{\kappa}\right) C_p(X;\epsilon) + \ldots \tag{100}$$

where $C_{f,o} = 2\epsilon^2$ and $C_p(X;\epsilon)$ is a pressure coefficient based on reference conditions from the inviscid solution at the trailing edge. Equation (100) is a simple relation for the skin-friction coefficient in terms of the pressure coefficient. It is a direct requirement of matching and follows simply from the three-layer structure of turbulent boundary layers near trailing edges. It involves only two turbulence parameters $C_{f,o}$ and κ. The parameter $C_{f,o}$ is the skin coefficient upstream of the trailing edge and κ is the Karman constant which enters from the logarithmic term in the initial profile.

Although the skin-friction result was derived here in the context of the trailing-edge problem, it can be given a more general and useful interpretation. The three-layer structure of turbulent flows also appears to apply to situations with large imposed pressure gradients. In this case equation (100) is valid with $C_{f,o}$ identified with the skin-friction coefficient upstream of the large-pressure-gradient region. The pressure coefficient is then defined with respect to reference quantities at the beginning of the pressure change. To check these concepts the skin-friction coefficient predicted by equation (100) was compared with data of Schubauer and Klebanoff (ref. 18). In reference 18 Schubauer and Klebanoff measured the skin-friction and pressure distributions in turbulent boundary layers approaching separation in a moderately large adverse pressure gradient. The skin-friction coefficient was computed by using the experimentally determined pressure coefficient in equation (100). The results are compared with the data in figure 25. Comparisons with the turbulent boundary computations of Bradshaw, Ferris, and Atwell (ref. 30) obtained with a turbulent energy approach are also included.

In this figure the combination $1 - C_p(X;\epsilon)$ is referred to as the first term. This one-term solution is equivalent to the assumption of a constant local skin-friction coefficient (i.e., a skin-friction coefficient based on the local dynamic pressure at the edge of the boundary layer). This result correctly indicates the main trend of the skin-friction variation with pressure but is in relatively poor agreement with the data. The inclusion of the logarithmic term in the solution greatly improves the agreement with the experimental data.

The numerical solutions given in figure 25 were obtained with and without a curvature correction. The present results should be compared with the numerical solution without the correction since it is not included in the present results. The agreement with the uncorrected numerical solution is seen to be quite good throughout the pressure rise. The better agreement with the experimental data and with the corrected numerical solution is probably fortuitous. However, the comparisons in figure 25 clearly indicate that the logarithmic interaction term is large and that very good results are obtained with its inclusion. These results also suggest that equation (100) can be made the basis of a separation criteria. The comparisons given tend to confirm the multilayer structure of turbulent flows proposed in the present study.

Concluding Remarks

In the present investigation a formal asymptotic description of turbulent interactions at airfoil trailing edges was developed. The most important result of the present study was the formulation of a boundary-value problem that governs the solutions for the interaction pressure distribution and lift coefficient on an airfoil. The interaction can be described as an inviscid rotational flow governed by a linearized Poisson equation. Work is currently in progress to complete the solution of these equations. Also the analysis has recently been extended to compressible flow and it has been demonstrated that the basic formulation applies to the case with minor modification provided the Mach number near the trailing edge is less than one. Both of these developments will be described in future publications on the subject.

The results discussed in this section are concerned with the lifting, basically antisymmetric problem. The effect of wake-induced displacement pressures, which was so important in the laminar problem, is absent to the order of the small parameter ϵ considered so far in the turbulent problem. The present solutions can be carried to higher order in ϵ. The next terms in the series are likely to the order of $\epsilon^2 \ln \epsilon$ and ϵ^2. These terms involve the thickness effects of the boundary layers on the airfoil and in the wake. However, the resulting problem is symmetric and so the solution would not affect the lift coefficient to this order. The major unsolved aspects of the problem concern the structure of the expansions in the inner layers of the wake. Further analysis is required to clarify the nature of the solution of this complex problem.

APPENDIX

THE SIMILARITY FUNCTIONS

The function $F_1(\eta)$ arising in the symmetric problem for X large and negative satisfies the differential equation and boundary conditions

$$F_1''' - 18\eta^2 F_1'' - 36\left(\eta F_1' - F_1\right) = -2^{5/3}3^{-1/2} \tag{A1a}$$

$$F_1(0) = F_1'(0) = 0 \qquad F_1''(\eta) \to 0 \qquad (\eta \to \infty) \tag{A1b}$$

It follows that

$$F_1 \to \left[3^{-7/6}(1/3)!/(-1/3)!\right]\eta \qquad (\eta \to \infty) \tag{A1c}$$

The functions $H_i(\eta)$ arising in the angle-of-attack problem for X large and negative satisfy the differential equations and boundary conditions

$$H_i''' - 18\eta^2 H_i'' + 9(4 - i)\left(\eta H_i' - H_i\right) = h_i \tag{A2a}$$

$$H_i(0) = H_i'(0) = 0 \qquad H_i''(\eta) \to 0 \qquad (\eta \to \infty) \tag{A2b}$$

where

$$h_1 = 9/2^{1/3} \tag{A2c}$$

$$h_2 = \left(3/2^{1/3}\right)\left(3H_1H_1'' - H_1'^2\right) \tag{A2d}$$

$$h_3 = \left(3/2^{1/3}\right)\left(2H_1''H_2 - H_2'H_1' + 3H_2''H_1\right) \tag{A2e}$$

It can be shown that the $H_i(\eta)$'s have the following asymptotic behavior for

$$H_1 = \tfrac{2}{3}C_{11}\eta^{3/2} + C_{12}\eta + C_{13} + \ldots \tag{A3a}$$

$$H_2 = C_{21}\eta \ln \eta + C_{22}\eta + C_{23}\eta^{1/2} + C_{24} + \ldots \tag{A3b}$$

$$H_3 = C_{31}\eta^{1/2} \ln \eta + C_{32} \ln \eta + C_{33}\eta + C_{34}\eta^{1/2} + C_{35} + \ldots \tag{A3c}$$

where the constants C_{ij} have been determined from analytical studies in references 1 to 3 and from numerical solutions obtained in the present investigation to be

$$\left.\begin{array}{lll} C_{11} = -3(2)^{1/6}(-2/3)!/(1/6)! & C_{12} = 6^{1/3}(-1/3)! & C_{13} = -1/K \\ C_{21} = -3.255 & C_{22} = 3.082 & C_{23} = C_{11}C_{22}/K \\ C_{24} = C_{12}^2/2K & C_{31} = C_{11}C_{21}/K & C_{32} = C_{12}C_{21}/K \\ C_{33} = -17.408 & C_{34} = 16.900 & C_{35} = (C_{21} + C_{22})C_{12}/K \end{array}\right\} \quad \text{(A4)}$$

where $K = 3(2)^{1/3}$.

The function $G_o(\eta)$ governing the trailing-edge behavior satisfies the following differential equations and boundary conditions:

$$G_o''' + 2G_oG_o'' - G_o'^2 = 27(2)^{4/3}C_o \qquad \text{(A5a)}$$

$$G_o'(\eta) - 18\lambda_{1,T}\eta = D_T - 0 \qquad (\eta \to \infty) \qquad \text{(A5b)}$$

$$G_o'(\eta) - 18\lambda_{1,B}\eta = D_B - 0 \qquad (\eta \to -\infty) \qquad \text{(A5c)}$$

where $\lambda_{1,T}$ and $\lambda_{1,B}$ are the values of the skin friction $\partial U/\partial Z\big|_T$ and $\partial U/\partial Z\big|_B$ at the trailing edge and C_o is a constant to be determined as part of the solution. Further details, together with typical solutions, are given in references 3 and 23.

REFERENCES

1. Stewartson, K.: On the Flow Near the Trailing Edge of a Flat Plate II. Mathematika, vol. 16, 1969.

2. Messiter, A. F.: Boundary Layer Flow Near the Trailing Edge of a Flat Plate. SIAM J. Appl. Math., vol. 18, 1970.

3. Brown, S. N.; and Stewartson, K.: Trailing Edge Stall. J. Fluid Mech., vol. 42, 1970.

4. Keller, H.: A New Difference Scheme for Parabolic Problems. Numerical Solutions of Partial Differential Equations, J. Bramble, ed., Academic Press, New York, 1970.

5. Keller, H.; and Cebeci, T.: Accurate Numerical Methods for Boundary Layer Flows. II: Two-Dimensional Turbulent Flows. AIAA J., vol. 10, no. 9, 1972.

6. Jobe, C. E.; and Burggraf, O. R.: The Numerical Solutions of the Asymptotic Equation of Trailing Edge Flow. Proc. Royal Soc. London, A340, 1974. (See ref. 26.)

7. Veldman, A. E. P.; and Van De Vooren, A. I.: Drag of a Finite Flat Plate. Proceedings of the Fourth International Conference Numerical Methods in Fluid Dynamics. Volume 35 of Lecture Notes in Physics, Springer-Verlag, 1975.

8. Janour, Z.: Resistance of a Flat Plate at Low Reynolds Numbers. NACA TM 1316, 1951.

9. Sato, H.; and Kuriki, K.: The Mechanism of Transition in the Wake of a Thin Plate Placed Parallel to a Uniform Flow. J. Fluid Mech., vol. 11, 1961.

10. Spence, D. A.: Wake Curvature and the Kutta Condition. J. Fluid Mech., vol. 44, 1970.

11. Küchman, D.: Inviscid Shear Flow Near the Trailing Edge of an Airfoil. Z. Flugwiss, vol. 15, 1967.

12. Mellor, G. L.: The Large Reynolds Number Asymptotic Theory of Turbulent Boundary Layers. Int. J. Eng. Sci., vol. 10, 1972.

13. Yajnik, K.: Asymptotic Theory of Turbulent Shear Flows. J. Fluid Mech., vol. 42, 1970.

14. Bush, W. B.; and Fendell, F.: Asymptotic Analysis of Turbulent Channel and Boundary Layer Flow. J. Fluid Mech., vol. 56, 1972.

15. Bush, W. B.; and Fendell, F.: Asymptotic Analysis of Turbulent Channel Flow for Mean Turbulent Energy Closures. Phys. Fluids, vol. 16, 1973.

16. Melnik, R. E.; and Grossman, B.: Analysis of the Interaction Between a Weak Normal Shock Wave With a Turbulent Boundary Layer. AIAA Paper 74-598, 1974.

17. Adamson, T. C., Jr.; and Feo, A.: Interactions Between a Shock Wave and a Turbulent Boundary Layer in Transonic Flow. SIAM J. App. Math., vol. 29, no. 1, July 1975.

18. Schubauer, G.; and Klebanoff, P. S.: Investigation of Separation of the Turbulent Boundary Layer. NACA Rep. 1030, 1951. (Supersedes NACA TN 2133.)

19. Van Dyke, M. D.: Higher Order Boundary Layer Theory. Annual Review of Fluid Mechanics, vol. 1, 1969, pp. 265-292.

20. Stewartson, K.: Multistructural Boundary Layers. Advances in Appl. Mech., vol. 14, 1974, pp. 145-239.

21. Goldstein, S.: Concerning Some Solutions of Boundary Layer Equations in Hydrodynamics. Proc. Cambridge Phil. Soc., vol. 26, 1930.

22. Goldburg, A.; and Cheng, S. I.: An Anomaly in the Application of Poincare-Lighthill-Kuo and Parabolic Coordinates to the Trailing Edge Boundary Layer. J. Math. Mech., vol. 10, 1961.

23. Hakkinen, R. J.; and Rott, N.: Similar Solutions for Merging Shear Flows. AIAA J., vol. 3, 1965.

24. Ackerberg, R. C.; and Phillips, J. H.: A Numerical Method for Highly Accelerated Laminar Boundary-Layer Flows. SIAM J. Numer. Anal., vol. 10, 1973.

25. Schneider, L. I.; and Denny, V. E.: Evolution of the Laminar Wake Behind a Flat Plate and Its Upstream Influence. AIAA J., vol. 9, 1971.

26. Jobe, C. E.: The Numerical Solution of the Asymptotic Equations of Trailing Edge Flow. Ph. D. Diss., The Ohio State University, 1973.

27. Stewartson, K.: On the Asymptotic Theory of Separated and Unseparated Fluid Motions. SIAM J. Appl. Math., vol. 28, no. 2, 1975.

28. Lighthill, M. J.: On Boundary Layers and Upstream Influence. II: Supersonic Flows Without Separation. Proc. Royal Soc. London, Ser. A, vol. 217, 1953.

29. Townsend, A. A.: Equilibrium Layers and Wall Turbulence. J. Fluid Mech., vol. 11, 1961.

30. Bradshaw, P.; Ferris, D. H.; and Atwell, N. P.: Calculation of Boundary-Layer Development Using the Turbulent Energy Equation. J. Fluid Mech., vol. 28, 1967.

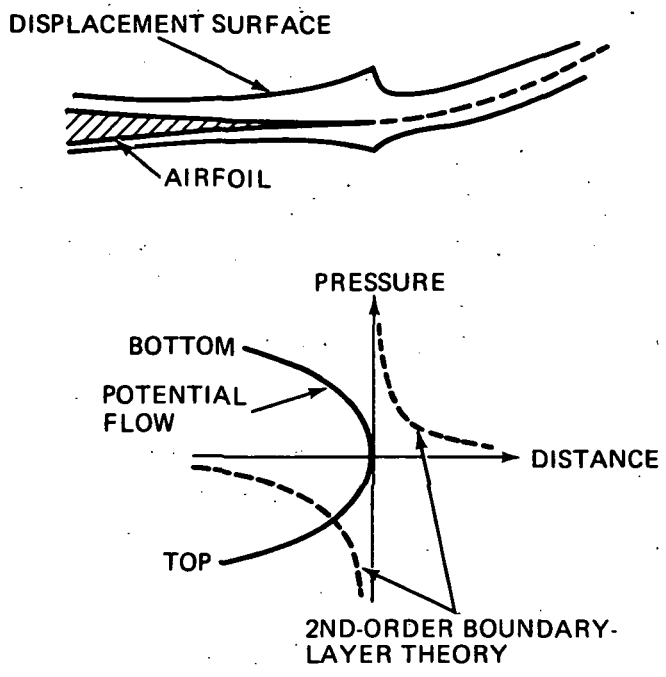

Figure 1.- Trailing-edge flow.

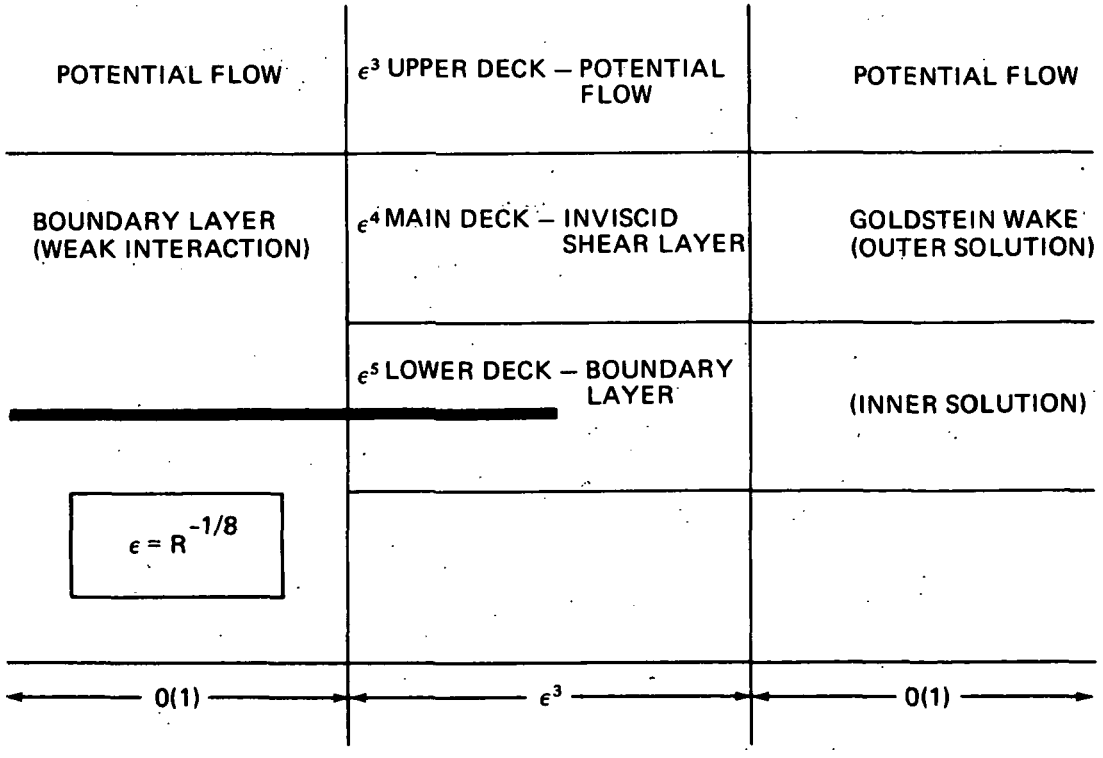

Figure 2.- Triple-deck structure.

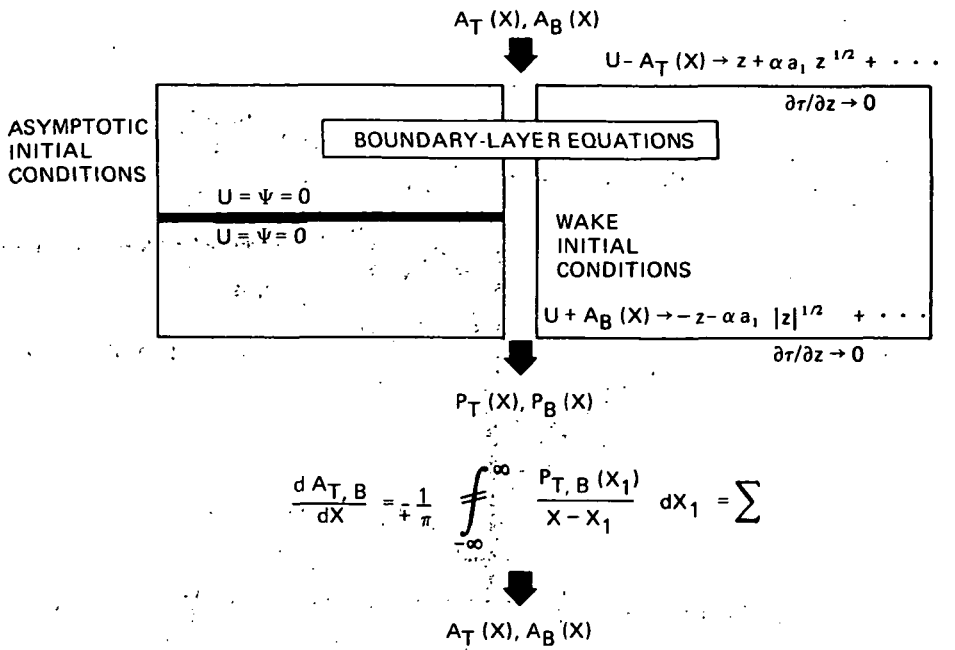

Figure 3.- Boundary-value problem for triple-deck solution.

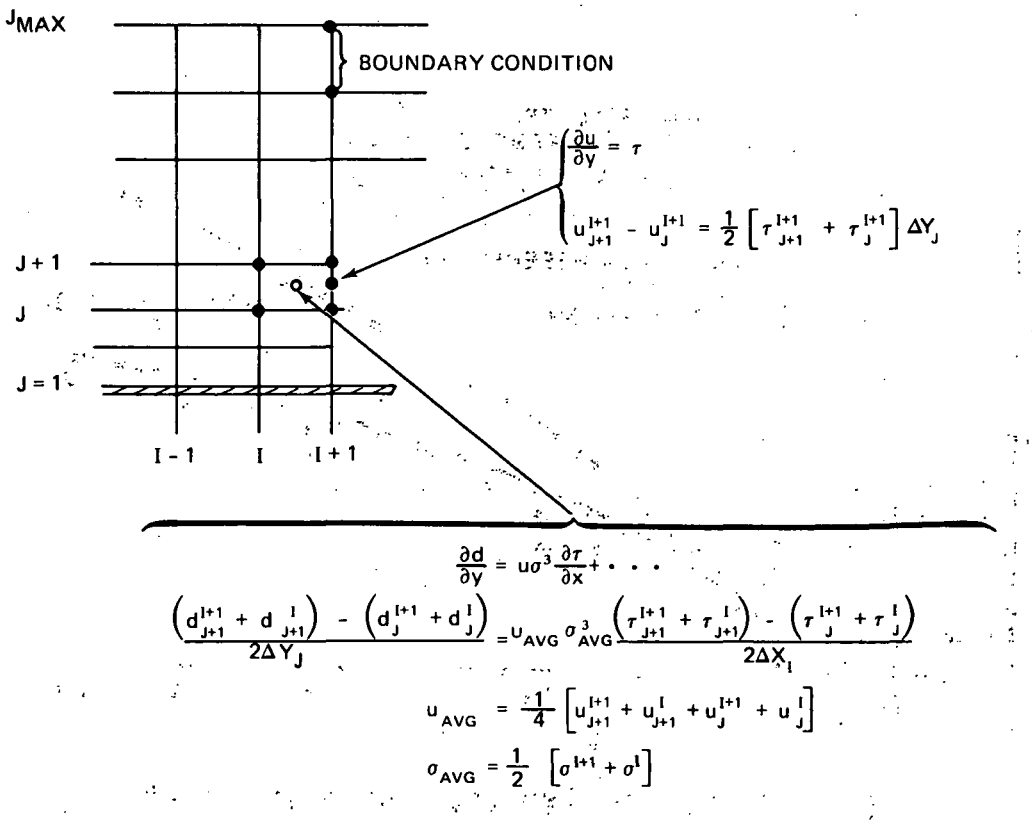

Figure 4.- Finite-difference approximation ("box" scheme).

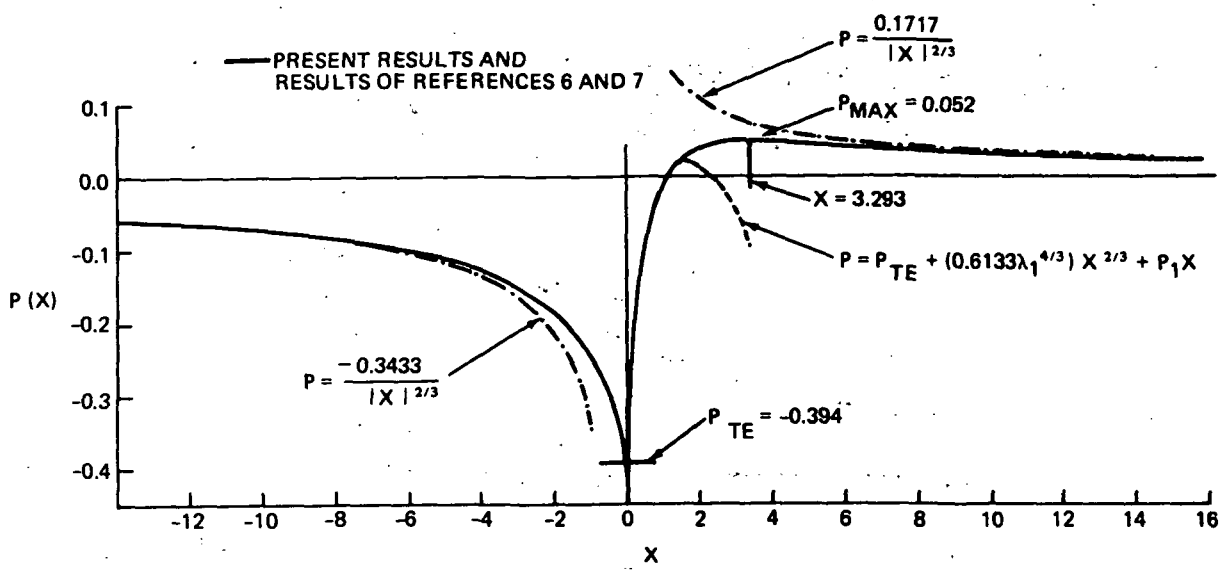

Figure 5.- Surface pressure distribution; $\alpha = 0$.

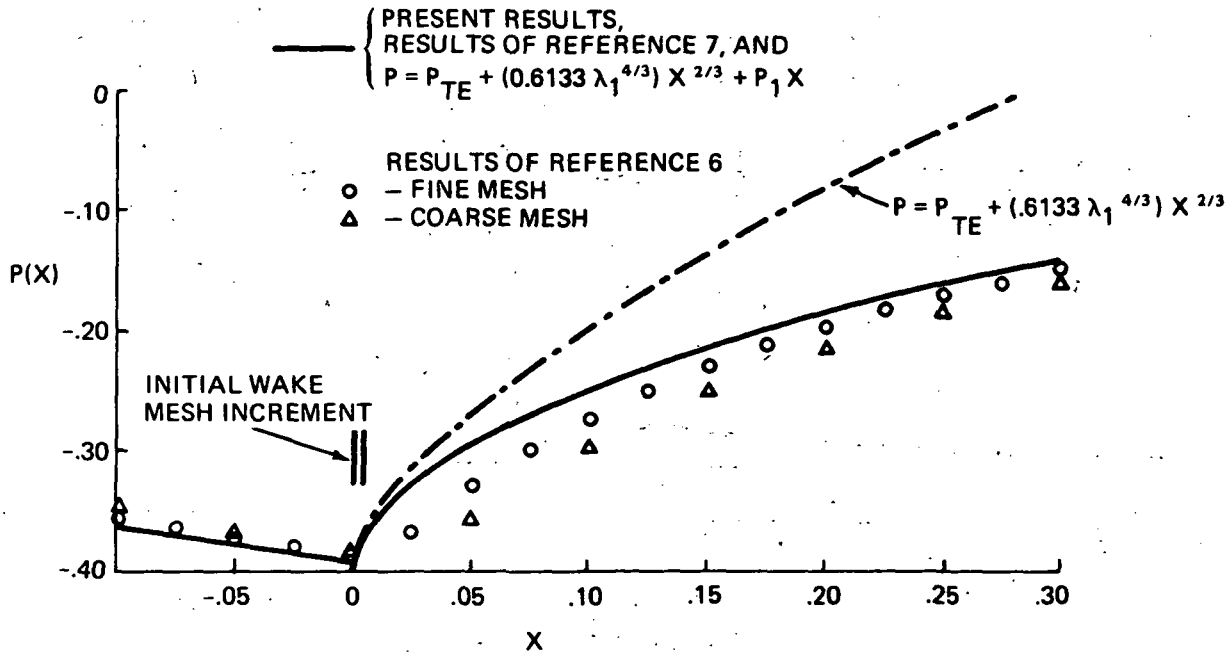

Figure 6.- Pressure distribution near origin; $\alpha = 0$.

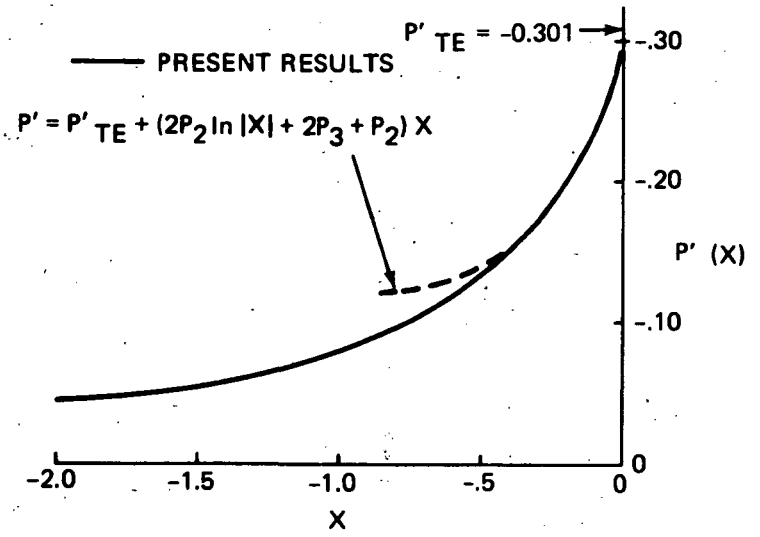

Figure 7.- Pressure gradient on plate near origin; $\alpha = 0$.

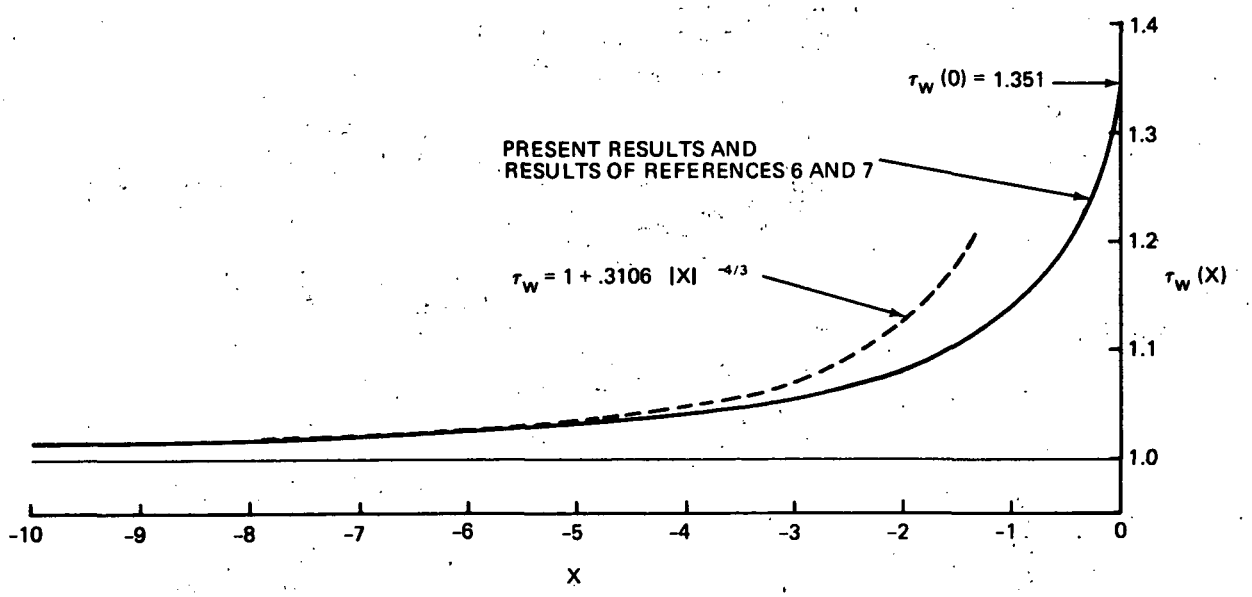

Figure 8.- Skin friction; $\alpha = 0$.

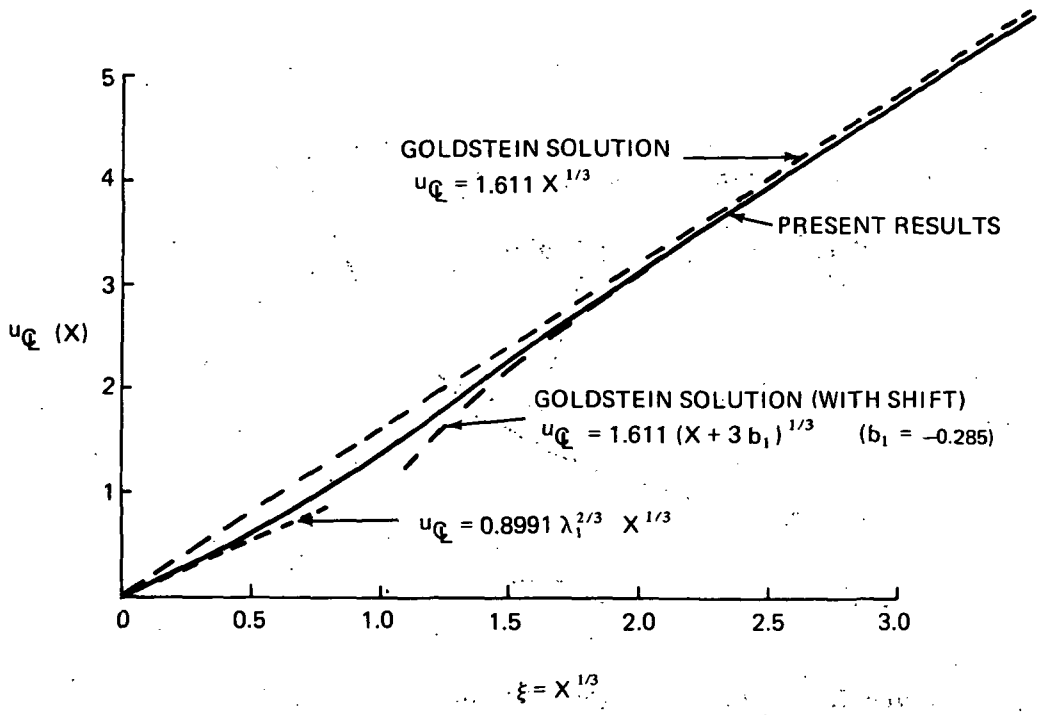

Figure 9.- Comparison of centerline velocity with singular solutions for $X \to 0$ and for $X \to \infty$; $\alpha = 0$.

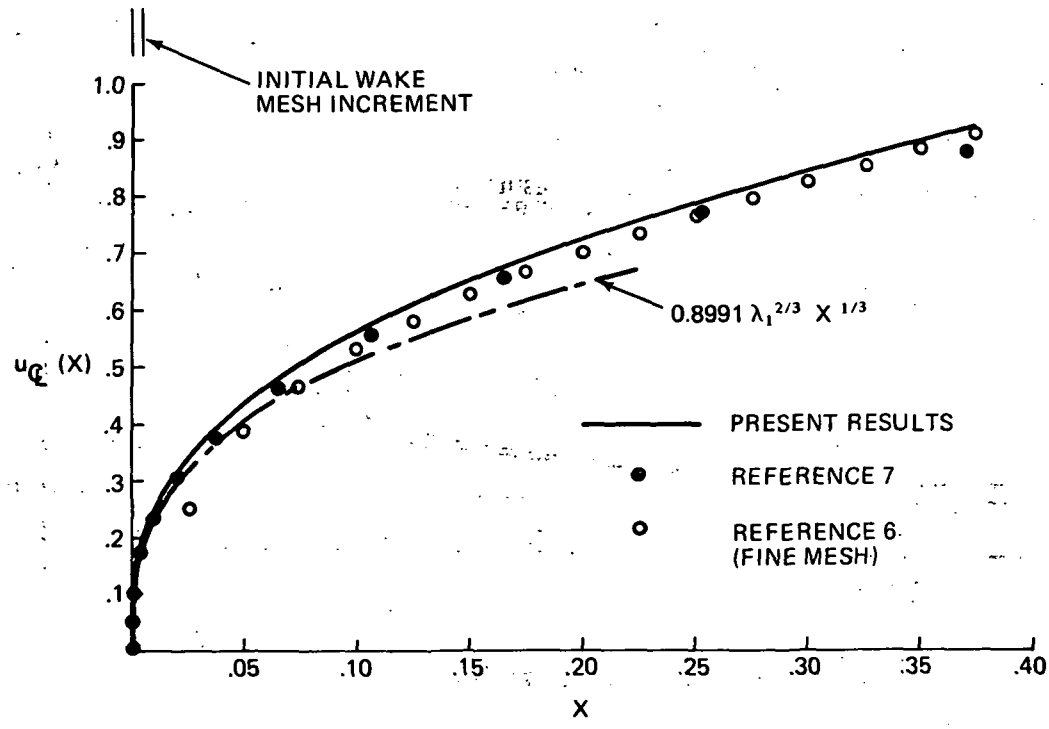

Figure 10.- Centerline velocity near origin; $\alpha = 0$.

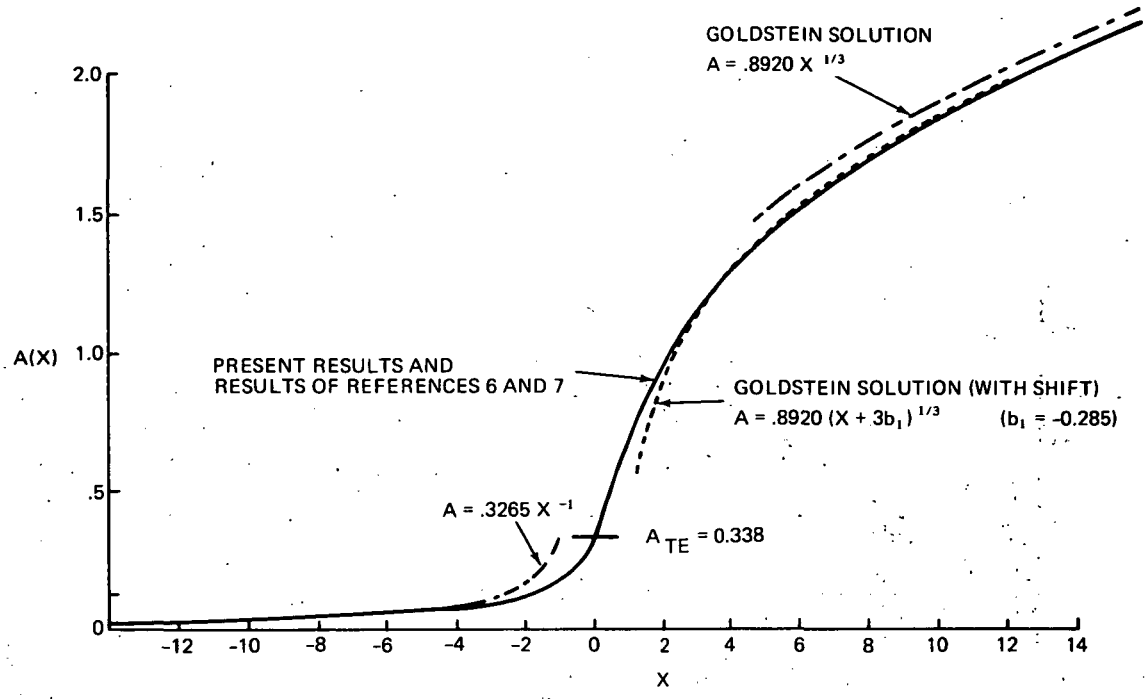

Figure 11.- Displacement function; $\alpha = 0$.

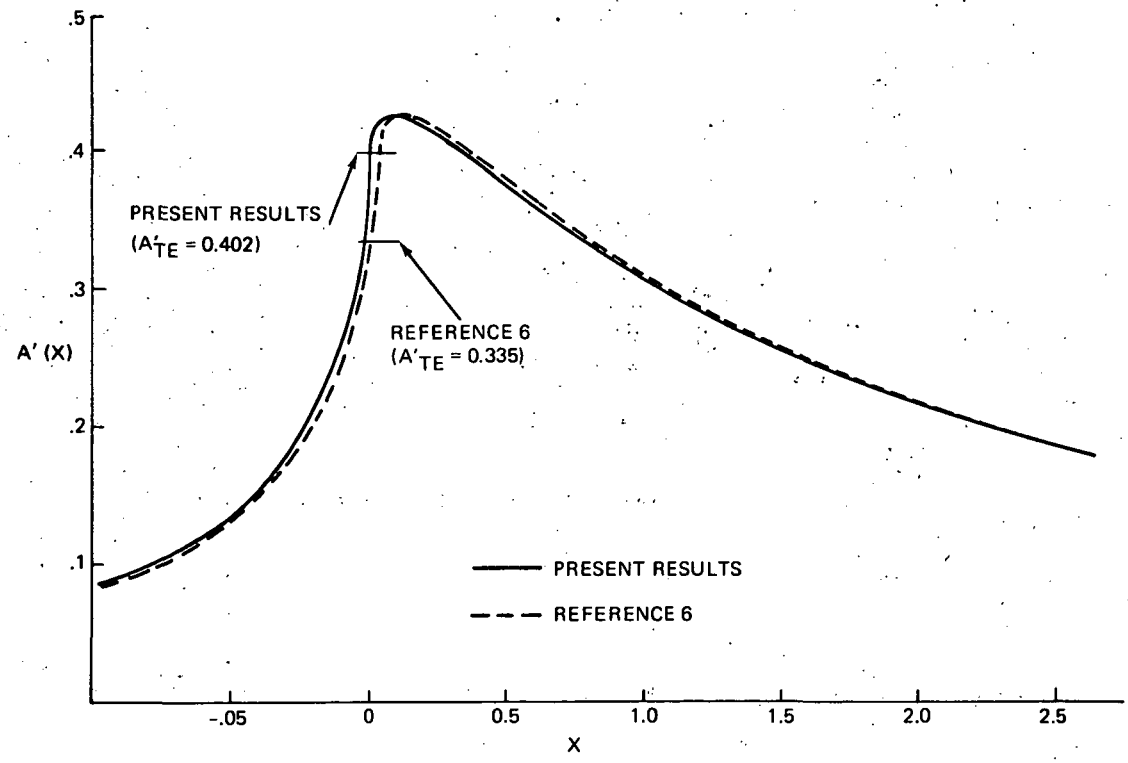

Figure 12.- Displacement surface slope A'(X); $\alpha = 0$.

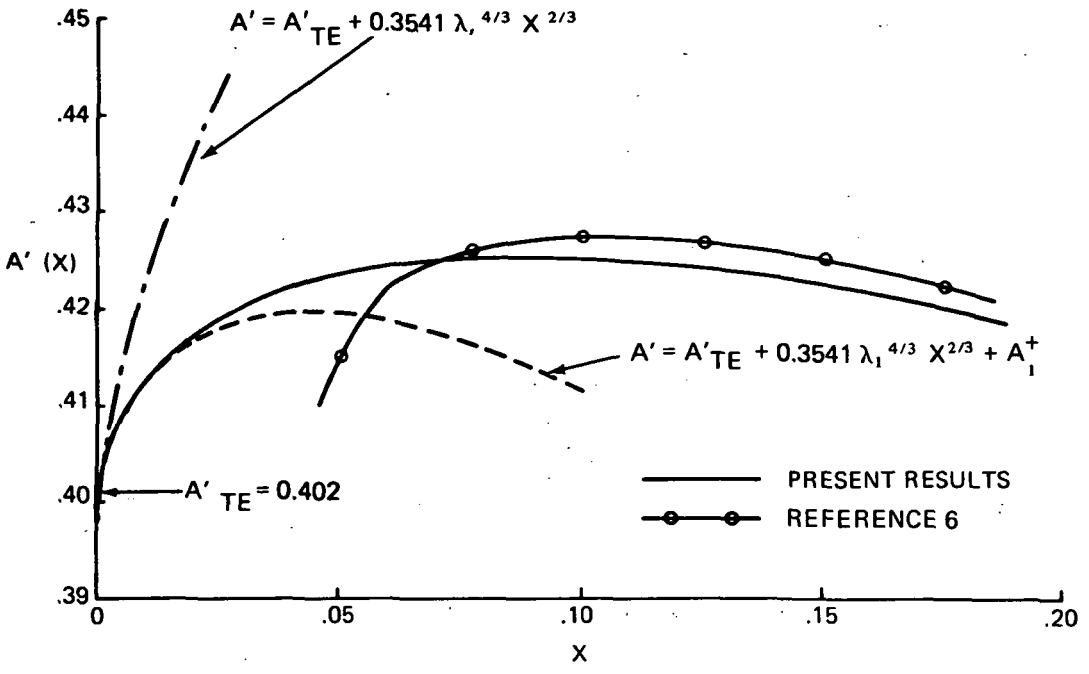

Figure 13.- Behavior of slope function near origin; $\alpha = 0$.

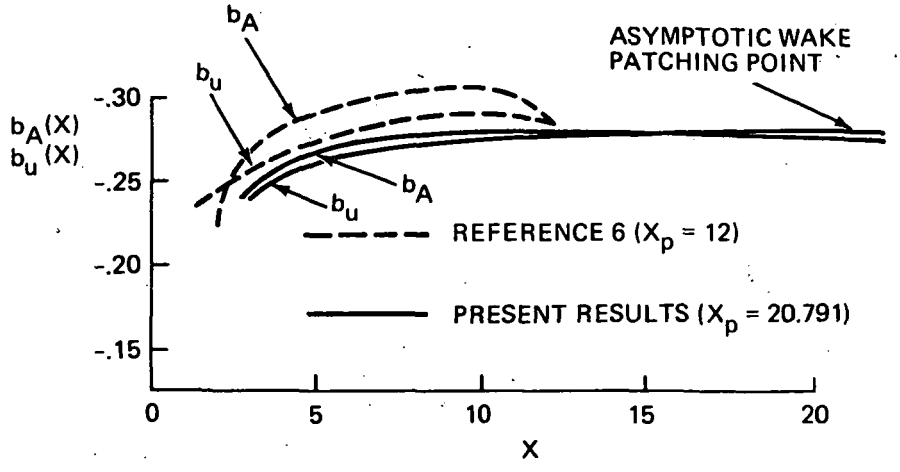

Figure 14.- Asymptotic behavior for large positive X; $\alpha = 0$.

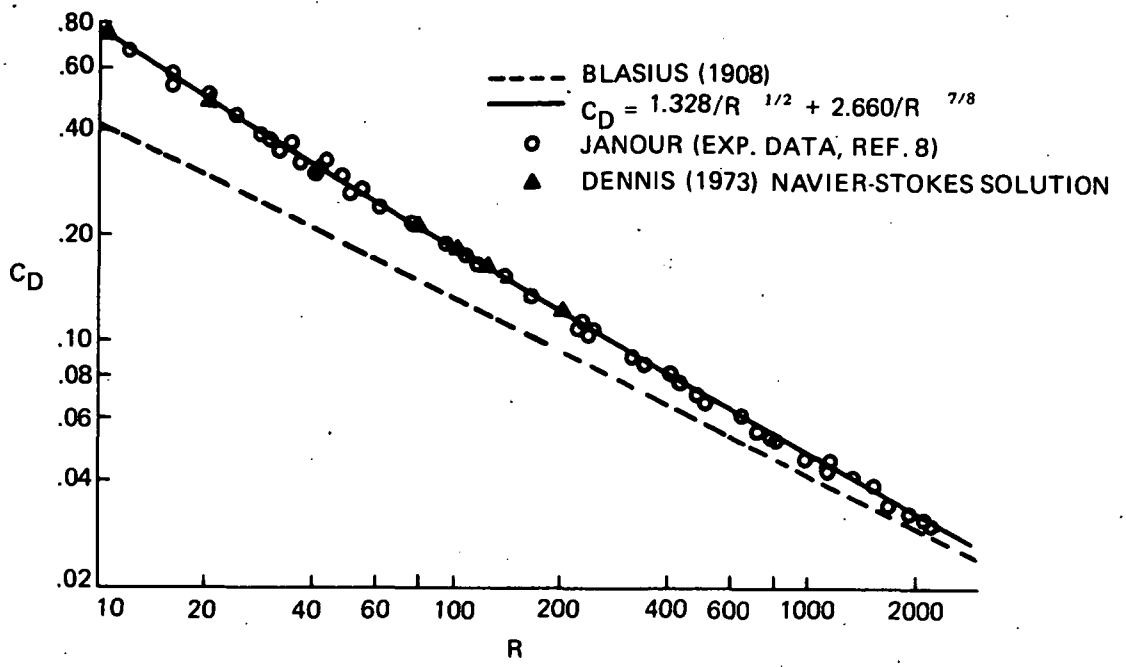

Figure 15.- Drag of finite flat plate as a function of Reynolds number at zero angle of attack.

						∞		
R	40	75	100	125	150	REF. 6	REF. 7	PRESENT
d_2	2.546	2.609	2.632	2.646	2.655	2.694	2.651	2.660

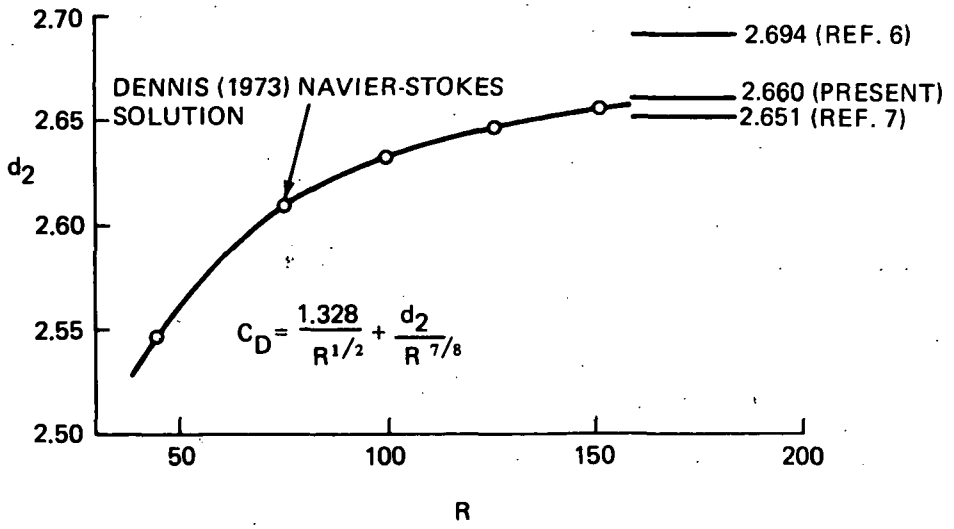

Figure 16.- Comparison between triple-deck and Navier-Stokes solutions for drag constant.

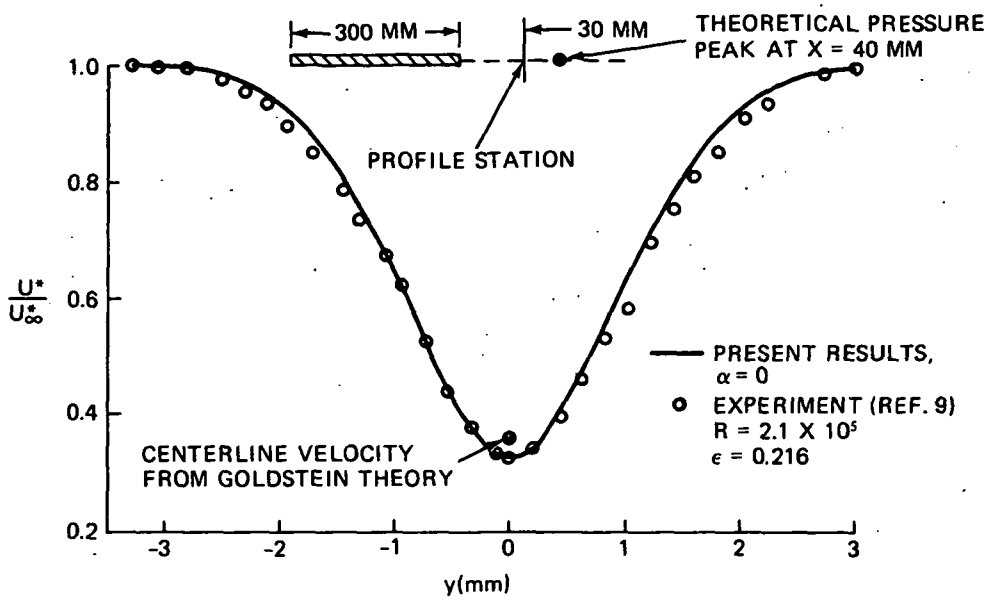

Figure 17.- Comparison of triple-deck velocity profile in wake of symmetric plate with data of Sato and Kuriki (ref. 9).

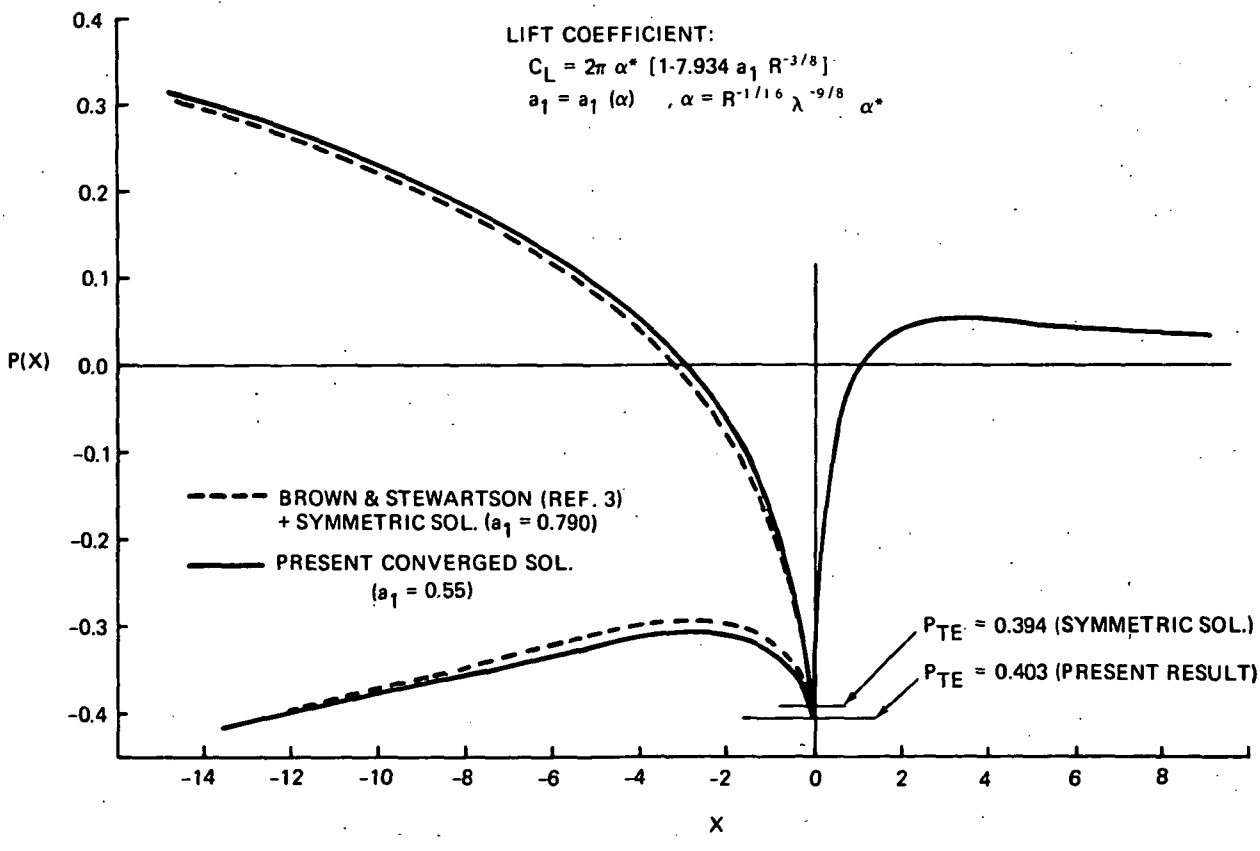

Figure 18.- Comparison of present solution with linearized solution of reference 3; $\alpha = 0.1$.

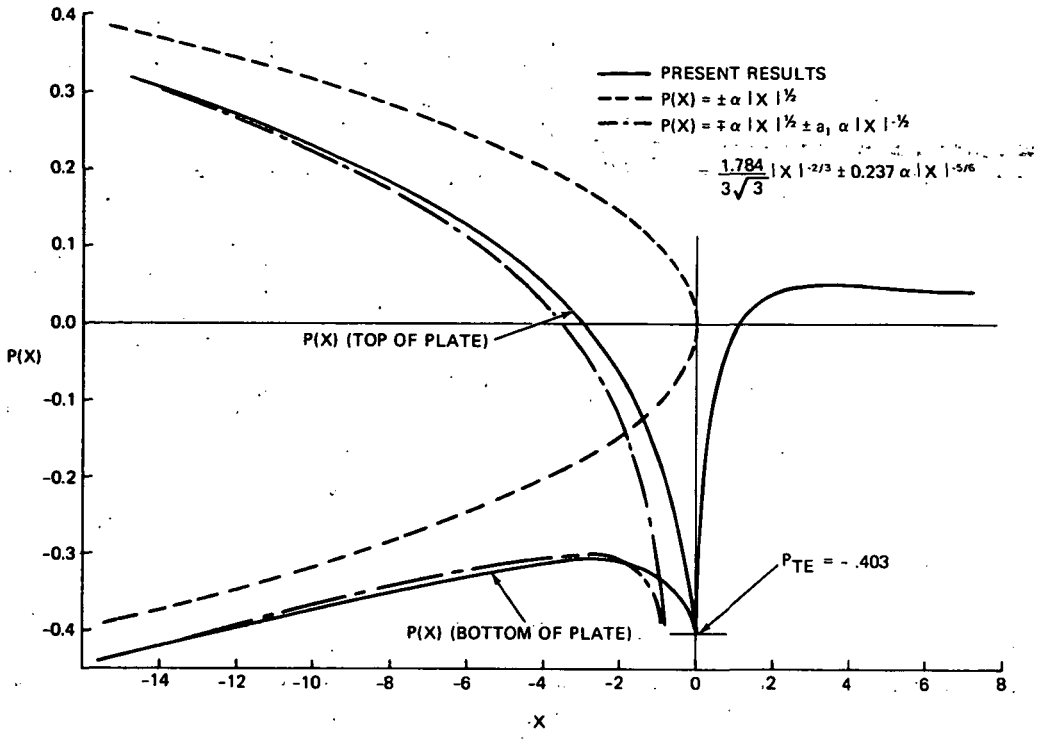

Figure 19.- Surface pressure distribution; $\alpha = 0.1$.

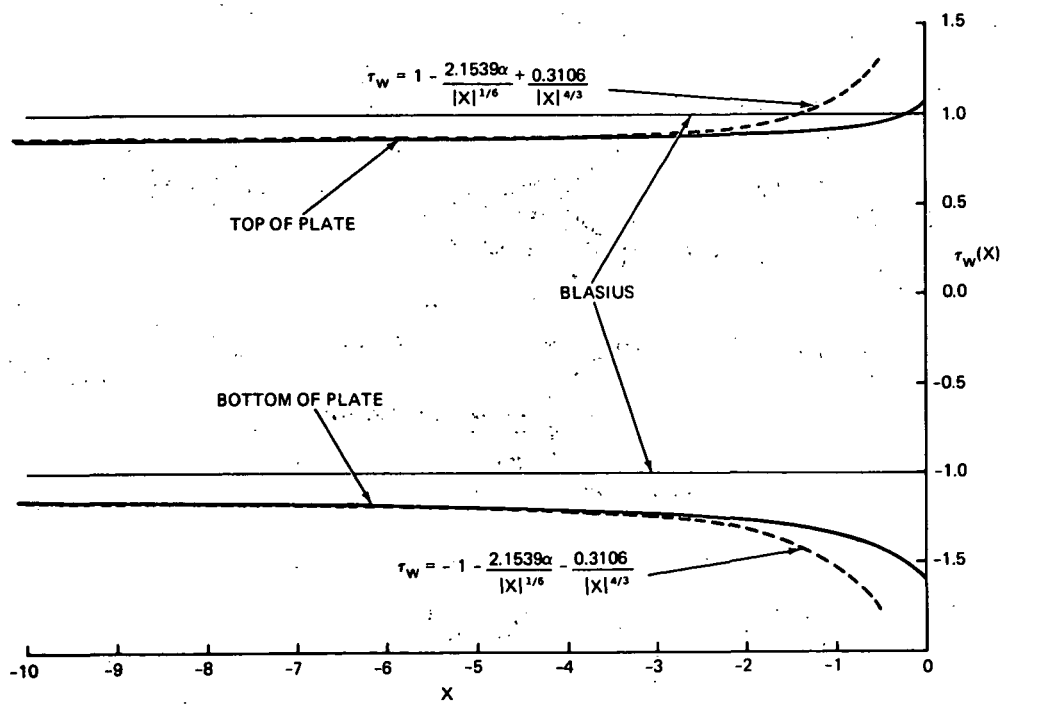

Figure 20.- Skin friction; $\alpha = 0.1$.

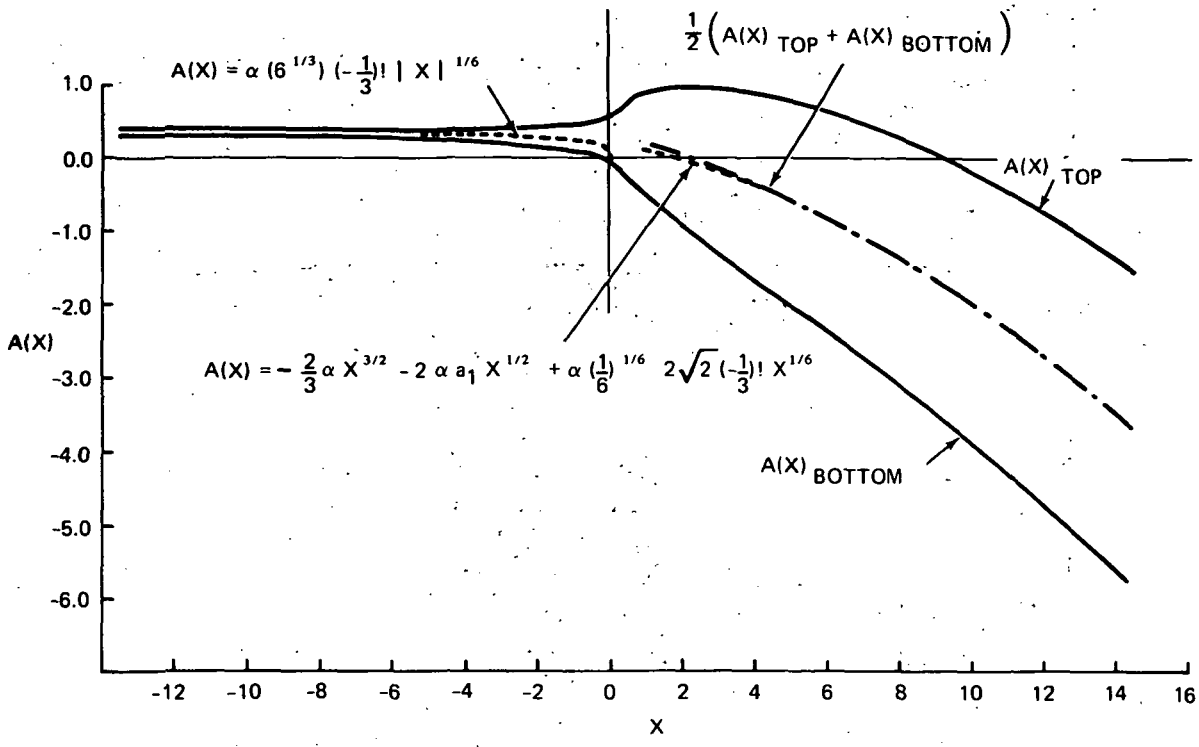

Figure 21.- Displacement function; $\alpha = 0.1$.

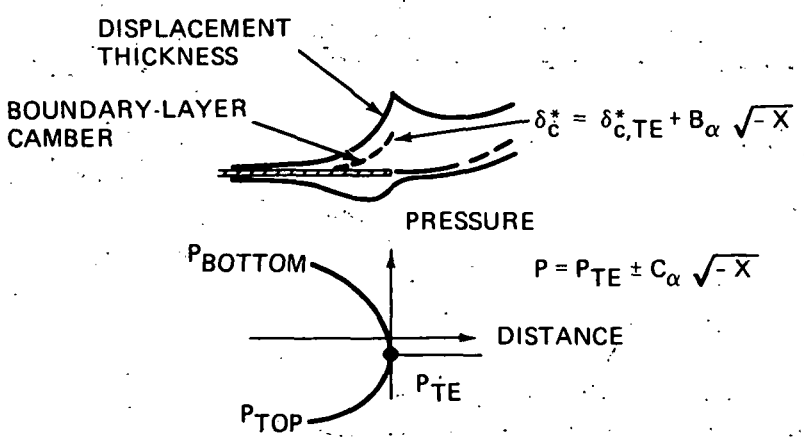

2ND-ORDER BOUNDARY-LAYER SOLUTION:

$$u = u_{TE} \pm C_\alpha \sqrt{-X} \pm \frac{\Delta\Gamma + D_\alpha \ln |X|}{\sqrt{-X}} + \cdots$$

Figure 22.- Second-order boundary-layer theory – turbulent flow.

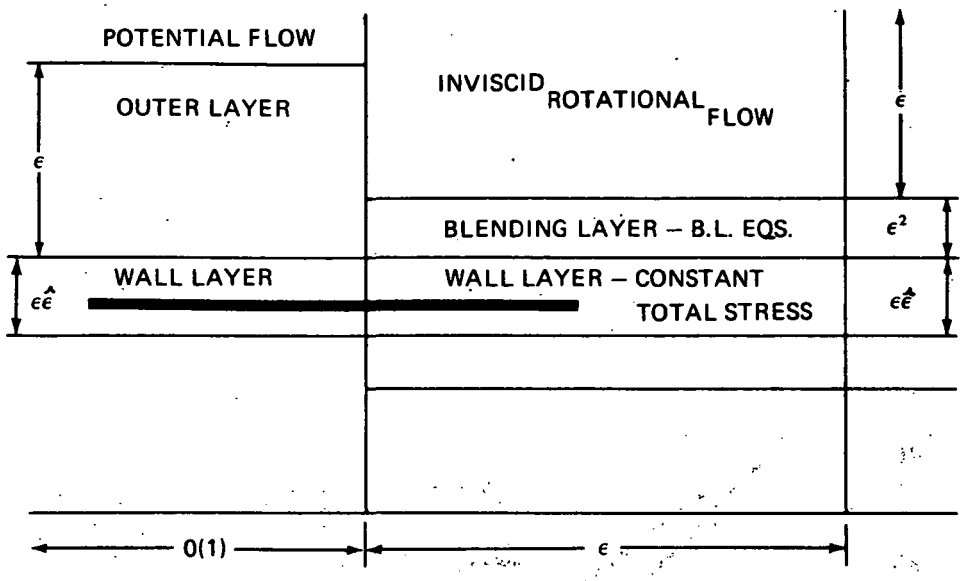

$\epsilon = \sqrt{C_{f,o}/2}$ (FRICTION VELOCITY)

$\hat{\epsilon} = (\epsilon^2 R)^{-1}$

LIMIT: $\epsilon \to 0 \quad (R \to \infty)$

Figure 23.- Flow field structure – turbulent interaction.

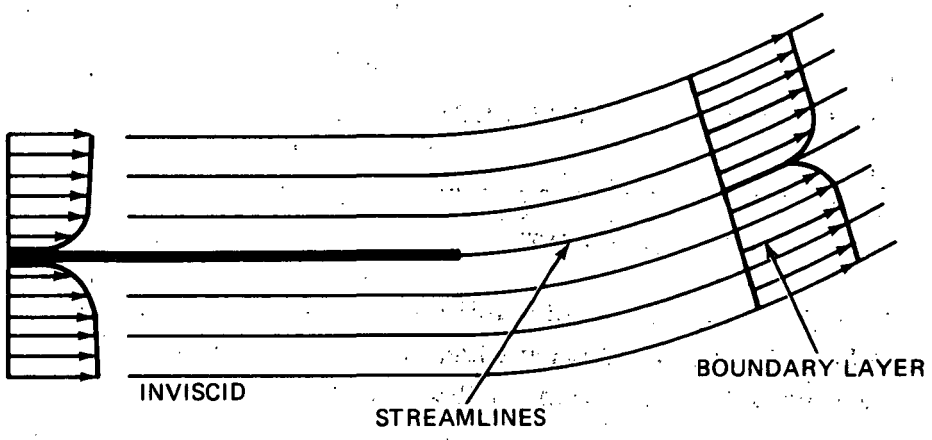

$$\psi = \psi_{INV} + \psi_{BL} + \psi'$$

$$\nabla^2 \psi' = \zeta(x, y) = -u_{BL}(y)\, \psi_{INV}(x, y)$$

$$v' = \frac{\partial \psi'}{\partial X} \text{ (DOWNWASH VELOCITY)}$$

SOLUTION YIELDS: $C_L = 2\pi\alpha [\, 1 + a_1 \epsilon^2 \ln \epsilon + a_2 \epsilon^2 \,]$

Figure 24.- Outer problem.

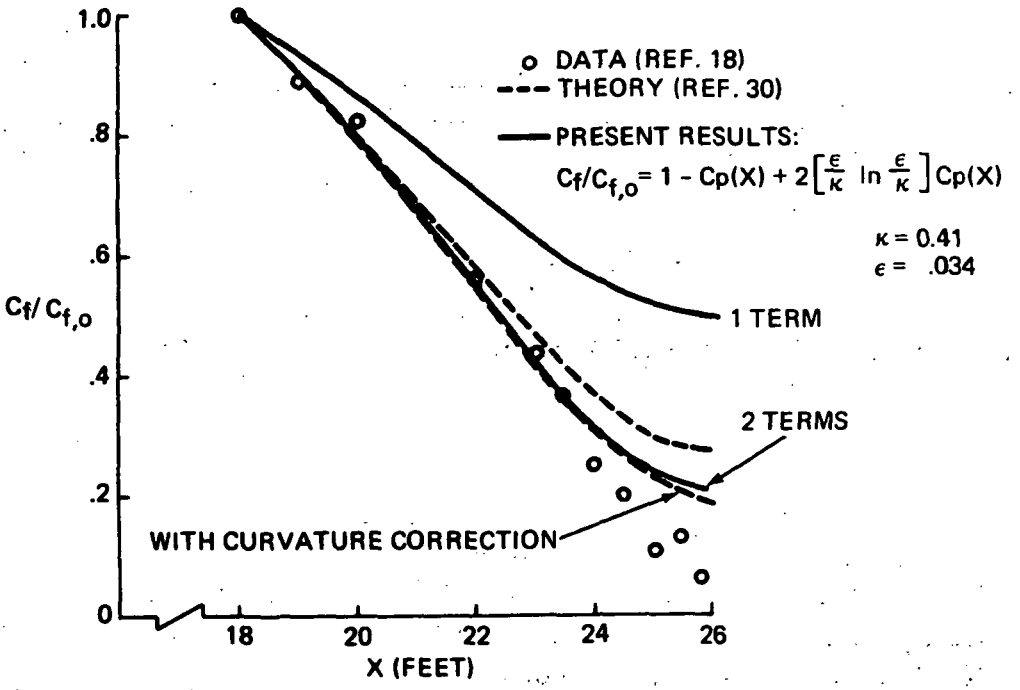

Figure 25.- Comparison of solution for skin friction with data of Schubauer and Klebanoff (ref. 18) and a turbulent boundary-layer solution. 1 ft = 0.3048 m.